Journal of Asian Earth Sciences 204 (2020) 104588

Contents lists available at ScienceDirect

Journal of Asian Earth Sciences

journal homepage: www.elsevier.com/locate/jseaes

Late Cretaceous calc-alkaline and adakitic magmatism in the Sistan suture zone (Eastern Iran): Implications for subduction polarity and regional tectonics

Michael Jentzer [a,*], Hubert Whitechurch [b], Philippe Agard [a], Marc Ulrich [b], Benoit Caron [a], Mohammad Hossein Zarrinkoub [c], Reza Kohansal [d], Lucie Miguet [a], Jafar Omrani [d], Marc Fournier [a]

[a] Sorbonne Université, CNRS, Institut des Sciences de la Terre de Paris (iSTeP), 4 place Jussieu 75005 Paris, France
[b] Université de Strasbourg, Ecole et Observatoire des Sciences de la Terre, Institut de Physique du Globe, Institut de Géologie, 1 rue Blessig, 67084 Strasbourg, France
[c] Department of Geology, University of Birjand, University Bd., Birjand, Southern Khorasan, Iran
[d] Geological Survey of Iran, Mehraj Bd., Tehran, Iran

ARTICLE INFO

Keywords:
Sistan orogeny
Calc-alkaline magmatism
Adakite
Iran geodynamics
Subduction

ABSTRACT

The N-S trendingSistan orogen (E Iran) stretches along ~700 km at a high angle compared to other Alpine-Himalayan ranges marking the Neotethyan suture (including the nearby Zagros, Makran or Alborz ranges). Both the geometry and timing of closure of the Sistan ocean are currently debated. We provide geochemical data on Late Cretaceous (~78 ± 8 Ma) magmatic samples collected on the eastern side of the Sistan suture zone. Petrography and major element compositions reveal two coexisting groups: a low-K calc-alkaline series with basaltic to rhyolitic composition, and a set of calc-alkaline intermediate to felsic samples. The low-K calc-alkaline series reflects classical arc magmatism and is characterized by negative anomalies in high field strength elements and positive anomalies in large ion lithophile elements. The calc-alkaline intermediate to felsic samples correspond to high-silica adakites characterized by strong positive anomalies in Sr and higher La/Yb ratios. Sr and Nd isotopic compositions of the low-K calc-alkaline series support partial melting of a DMM-like source contaminated by sediment-derived fluids, consistent with slab-dehydration in a juvenile subduction setting. An additional fraction of slab-derived melt is necessary to model trace element patterns of our adakites. Altogether, results indicate formation of a Late Cretaceous magmatic arc associated with NE-dipping subduction of the Sistan ocean below the stretched continental Afghan margin. The emplacement of adakites postdate the formation of the suture zone eclogites by a few Ma at most. Upwelling of hot asthenosphere following slab break-off would best explain the necessary warming-up of the subduction thermal regime.

1. Introduction

Orogenic calc-alkaline to alkaline magmatism relates to the subduction of oceanic lithosphere, before collision between continental margins (e.g., Martin and Piwinskii, 1972; Gill, 2012). As a result of Neotethyan closure, a wealth of calc-alkaline and alkaline magmatic rocks is exposed throughout the Iranian territory (Fig. 1a; e.g. Berberian and Berberian, 1981; Agard et al., 2011; Verdel et al., 2011), particularly in the Sistan region (E Iran) whose NS range strikes almost orthogonal to the adjacent Zagros, Makran or Alborz mountain ranges (Fig. 1a).

The Sistan orogen separates the Lut and Afghan continental blocks and stretches over ~ 700 km (Fig. 1a). The Sistan orogen hosts extensive, well-preserved Mesozoic ophiolites (Saccani et al., 2010; Zarrinkoub et al., 2012a), high-pressure and low-temperature (HP-LT) subduction remnants (Fotoohi Rad et al., 2005; Angiboust et al., 2013; Bröcker et al., 2013; Bonnet et al., 2018) and a profuse record of Mesozoic to Quaternary calc-alkaline to alkaline magmatism (Camp and Griffis, 1982; Pang et al., 2012, 2013).

Whether the Sistan ocean represents a back-arc domain and how (and if) this ocean was connected to the Neotethys is however unknown (Barrier et al., 2008, 2018; Saccani et al., 2010; Moghadam and Stern,

* Corresponding author.
E-mail address: michael.jentzer@sorbonne-universite.fr (M. Jentzer).

https://doi.org/10.1016/j.jseaes.2020.104588
Received 4 February 2020; Received in revised form 12 October 2020; Accepted 13 October 2020
Available online 20 October 2020

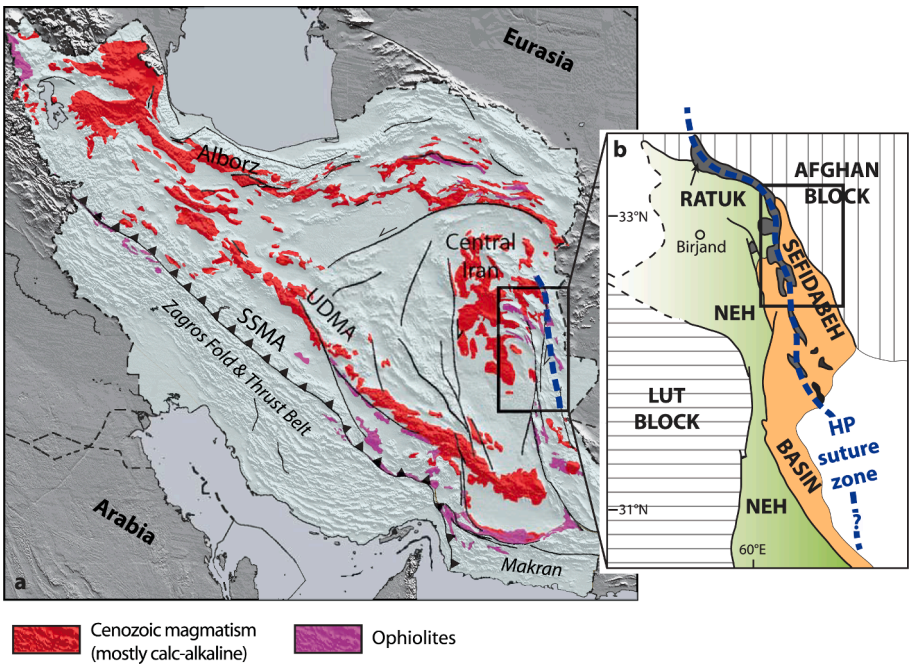

Fig. 1. Study location and regional context (a) Elevation map of Iran (modified after Paul et al., 2010) with the locations of the main Iranian magmatic provinces. SSMA and UDMA: Sanandaj–Sirjan and Urumieh–Dokhtar magmatic arcs (b) Schematic structure of the North Sistan belt.

2015). Similarly, the subduction polarity and the exact timing of oceanic convergence are presently debated: either to the NE below the Afghan block during the Campanian (Tirrul et al., 1983), to the SW below the Lut block during the Aptian (Pang et al., 2012) or both to the NE and SW below the Afghan and the Lut blocks during the Late Cretaceous (Arjmandzadeh et al., 2011). Although andesitic-like Late Cretaceous lavas have been reported in the eastern part of the belt, their geochemical signature remains unclear (i.e., calc-alkaline or tholeiitic; Tirrul et al., 1983; Maurizot et al., 1990a, 1990b; Zarrinkoub et al., 2012b). The aim of this contribution is therefore to provide detailed petrological and geochemical information, based on systematic sampling of these magmatic rocks, to constrain the closure of the Sistan oceanic domain.

2. Geological setting

2.1. Architecture and geodynamic evolution of the Sistan belt

The Sistan belt was mapped in 1977 and 1978 at 1:250.000 scale, as part of an extensive regional mapping and mineral exploration programme of the Geological and Mineral Survey of Iran. The first lithostratigraphic and tectonic frame was published by Tirrul et al. (1983), who recognized five main domains (Fig. 1b):

- (1) The Lut block to the W and (2) the Afghan block to the E, characterized by Neoproterozoic to Paleozoic basement (Stöcklin, 1968). The youngest sediments deposited on top of this basement prior to the Sistan orogeny are mildly deformed Jurassic series and Early Cretaceous (Barremian-Aptian) Orbitolina limestones.
- (3) The Neh Complex comprises weakly metamorphosed ophiolite nappes and ophiolitic mélanges together with low-grade metasedimentary rocks of Senonian age.
- (4) The Ratuk Complex is characterized by the presence of highly deformed ophiolitic mélanges and metasediments, locally metamorphosed under HP-LT conditions (Bonnet et al., 2018 and references therein).
- (5) The Sefidabeh basin, overlying both the Ratuk and Neh complexes, consists of Senonian to Eocene turbiditic sequences and was interpreted as deposited in a forearc basin.

Paleomagnetic data (Besse et al., 1998; Mattei et al., 2015) show that, prior to opening of the Sistan ocean, the Yazd, Tabas and Lut blocks underwent a similar counter-clockwise rotation of about 30° during the Jurassic, suggesting that they formed a single continental block in Central Iran at that time.

K-Ar dating of amphiboles from Sistan ophiolitic gabbros yielded an Aptian age of 124 ± 11 Ma (Delaloye and Desmons, 1980), while U-Pb dating of zircons from oceanic leucogabbros yielded an Albian age between 107 ± 1 and 113 ± 1 Ma (Zarrinkoub et al., 2012a). The Sistan oceanic basin was widely opened by the 'mid-'Cretaceous, at the time of deposition of the Orbitolina Limestone in Central Iran and in the Afghan block. Biostratigraphic dating of radiolarites overlying the ophiolites yielded Early Aptian to Late Albian ages (Babazadeh and De Wever, 2004; Ozsvárt et al., 2020), in agreement with radiochronometric dating. Babazadeh and De Wever (2004) suggested that the seafloor spreading of the Sistan ocean lasted from early to 'mid-'Cretaceous time. Berberian and Berberian (1981) proposed that the Sistan basin opened as a back-arc basin above the retreating Zagros subduction zone of the Neo-Tethys ocean, which was still active at that time. The paleogeographic orientation of the Sistan ocean is still largely speculative, ranging from N100 to N160°E (Saccani et al., 2010; Barrier et al., 2018).

Bröcker et al. (2013) used three methods to date the HP-LT metamorphic rocks along the Ratuk complex. Rb-Sr on phengite, glaucophane, omphacite, biotite, epidote, garnet, albite and garnet from eight samples yielded ages between 87.1 ± 0.3 and 84.9 ± 0.6 Ma for the mineral assemblages near the peak-T, while the retrograde assemblage yielded a younger age at 78.9 ± 0.5 Ma. ^{40}Ar-^{39}Ar plateau ages on five samples range between 87.6 ± 0.6 and 81.3 ± 1.3 Ma. U-Pb on zircons from four samples yielded ages between 89.3 ± 1.6 and 86.1 ± 1.1 Ma. Bonnet et al. (2018) provided fourteen Ar-Ar ages on phengite and amphibole. These ages range from 88.4 ± 0.35 to 83.81 ± 0.94 Ma without significant difference between the near peak-T and retrograde assemblages. Most dates for the Sistan high pressure metamorphism therefore lie between 89 and 83 Ma (i.e., Coniacian-Santonian), suggesting subduction of the Sistan ocean was in mature thermal state at the time. Thick deposits of Senonian (89 to 66 Ma) flysch also imply the presence of a highly subsiding basin, consistent with the existence of a nearby subduction zone (Tirrul et al., 1983). However, no related

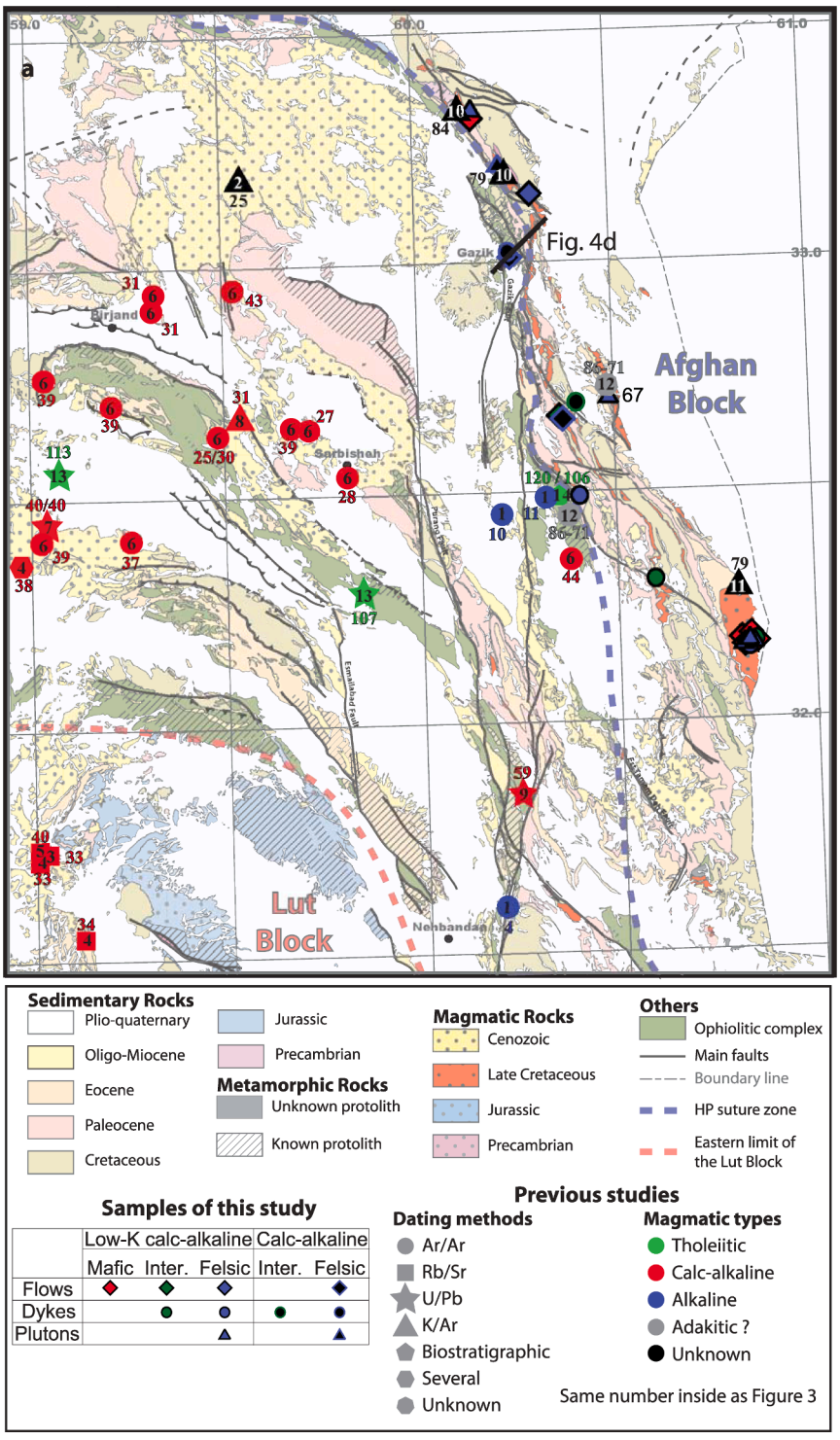

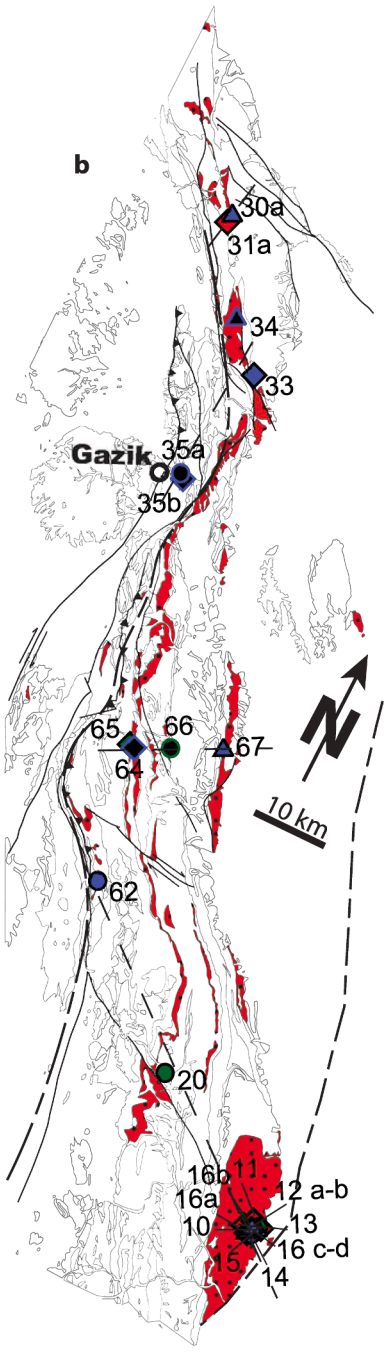

Fig. 2. (a) Structural map of the North Sistan belt with the location of our samples and the previous magmatic rocks studied. References: 01: Pang et al, 2013; 02: Fauvelet and Eftekhar-Nezhad, 1990; 03: Arjmandzadeh and Santos, 2014; 04: Karimpour et al.,2011; 05: Kluyver et al, 1978; 06: Pang et al, 2013; 07: Abdi and Karimpour, 2013; 08: Jung et al. 1983; 09: Delavari et al, 2014; 10: Maurizot et al., 1990b; 11: Maurizot et al., 1990a; 12: Zarrinkoub et al., 2012b; 13: Zarrinkoub et al, 2012a; 14: Babazadeh and De Wever, 2004. (b) Detail of the Late Cretaceous magmatic outcrops where our samples were collected.

magmatic activity has so far been reported.

Coarse-grained proximal molasse-type Eocene sediments overlying the flysch deposits constrain the onset of collision between the two continental blocks. Voluminous, mildly deformed syn- to post-collisional Paleogene magmatism cuts across the Lut block and part of the Sistan suture zone (Camp and Griffis, 1982). Ar-Ar age constraints for these magmatic rocks span the mid-Eocene (ca. 46 Ma) to Late Oligocene (ca. 25 Ma). This magmatism has been interpreted as the result of post-collisional lithospheric delamination (Pang et al., 2013).

During Miocene time, paleomagnetic data suggest a second 35° counter-clockwise rotation of Central Iran (Mattei et al., 2015). This rotation is accompanied by progressive activation of N-S right lateral

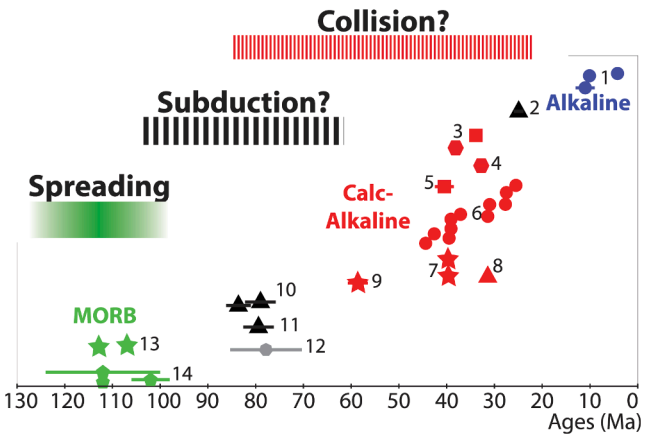

Fig. 3. Time evolution of the magmatism in the North Sistan area. Same legends than Fig. 2. Here, the uncertainties of each age are given by the length of the horizontal lines (more details in Table 1).

faults following the 60° counter-clockwise rotation of the main horizontal stress direction since the Late Miocene (Jentzer et al., 2017). The Sistan suture zone remains tectonically active at present, as shown by several morphologic indicators (e.g., shifts of river waterways) and by instrumental seismicity and paleoseismicity studies of strike-slip faults (e.g., N-S right lateral fault and their conjugate left lateral and NW-SE reverse faults; Berberian et al., 2000; Walker and Khatib, 2006). These strike-slip faults also acted as major pathways for the Late Cenozoic intraplate post-collisional alkali-basalts (ca. 27–2 Ma, K-Ar or Ar-Ar datings, Camp and Griffis, 1982; Pang et al., 2012; Walker et al., 2009).

2.2. Magmatic evolution of northern Sistan and subduction polarities

The age distribution of the Sistan magmatic rocks (Figs. 2 and 3 and Table 1) magmatic activity was almost continuous since the Early Cretaceous. Three main episodes corresponding to three distinct sets of rocks can be recognized:

(1) Ophiolitic magmatic rocks yielded U-Pb ages for two leucogabbros at 106.9 ± 1.1 and 112.8 ± 0.9 Ma (Albian; Zarrinkoub et al., 2012a). Radiolarian dating on cherts within the ophiolitic sequence gave Early Aptian (≈ 120 Ma) to Middle Albian (≈ 106 Ma) ages (Babazadeh and De Wever, 2004; Ozsvárt et al., 2020). Most magmatic rocks in the ophiolite have N-MORB characteristics, attributed to the partial melting of a depleted upper mantle. Associated E-MORB rocks have been related to partial melting of an enriched mantle in a supra-subduction zone setting (Saccani et al., 2010; Zarrinkoub et al., 2012a). Based on the E-MORB occurrences, Saccani et al. (2010) suggested the existence of a NE dipping intra-oceanic subduction zone.

(2) Calc-alkaline rocks such as basalt, andesite, dacite, rhyolite or rare granodiorite were dated from the Late Paleocene to Oligocene (ca. 59 to ca. 24 Ma; Abdi and Karimpour, 2013; Arjmandzadeh and Santos, 2014; Delavari et al., 2014; Jung et al., 1983; Karimpour et al., 2011; Kluyver et al., 1978; Pang et al., 2013; Fig. 2a and Table 1). This magmatism is volumetrically dominant in the region and largely extends to the W, outside the Sistan suture zone. Arjmandzadeh et al. (2011) related this calc-alkaline activity to two distinct E- and W-dipping long-lived subduction zones. Beydokhti et al. (2015) interpreted this Eo-Oligocene calc-alkaline magmatism as a marker of active westward subduction. Pang et al. (2013) and Omidianfar et al. (2020) related this magmatism to the partial melting of metasomatized lithospheric mantle following delamination of the lithospheric root and asthenospheric upflow during collision. For these authors, this delamination ensued after westward dipping subduction. In contrast, Camp and Griffis (1982) and Mohammadi et al. (2016) inferred a north-eastward dipping subduction beneath the Afghan Block at the end of the Cretaceous, based on the occurrence of calc-alkaline to tholeiitic lavas into Maastrichtian flysch sequences of southern Sistan. Tectono-stratigraphic and metamorphic studies rather advocate for eastward-dipping subduction at ~ 86 Ma (Tirrul et al., 1983; Angiboust et al., 2013; Bröcker et al., 2013; Bonnet et al., 2018).

(3) Miocene to Pliocene alkali basalts (mainly between ca. 11 and 4 Ma). They are emplaced along the main strike-slip faults and could result from the partial melting of the uprising asthenosphere after delamination of the lithospheric root (Pang et al., 2012).

Late Cretaceous magmatic rocks were less extensively studied. Three tonalitic rocks yield whole-rock K-Ar ages of 79.4 ± 3.2; 79.0 ± 3.2 and 83.6 ± 2.6 Ma (Maurizot et al., 1990a, 1990b). Six U-Pb dating of zircon from potentially adakitic granitoids located between W of Sulabest and Ratuk-e-Pa'in gave ages from 86.0 ± 0.8 to 71.5 ± 0.6 Ma (Zarrinkoub et al., 2010, 2012b; Figs. 2 and 3, Table 1). Given the lack of data on this crucial period for the evolution of the Sistan belt, these Late Cretaceous magmatic rocks are characterized below.

3. Sample characterization: location, age and petrology

3.1. Sampling strategy: Age and structural position

According to geological maps (Fig. 2), Late Cretaceous magmatic rocks crop out discontinuously in the NE Sistan belt over an area of 150 km from N to S, and 35 km from E to W. A line of positive aeromagnetic anomalies parallel to these outcrops suggests the presence of shallow magnetic bodies which may partly correspond to these igneous rocks (Yousefi and Friedberg, 1977). Twenty-three samples were collected along four E-W sections (dashed lines on Fig. 2b). Twenty-one samples were collected in the eastern part of the HP-LT Ratuk complex, in the Sefidabeh basin deposited onto the Afghan block (Fig. 4). Eleven of these samples come from the Cheshmeh-e Ostad Complex in the SE of the studied area. This complex provides the most extensive Late Cretaceous magmatic exposure and exhibits the greatest diversity of rock types.

Two samples (#35a and b) are from a tectonic unit flanking the western limit of the HP-LT domain (Figs. 2 and 4), likely equivalent to the "Western Unit" defined further south in the Sulabest area (Angiboust et al., 2013). The HP-LT units crop out in a tectonic window affected by younger deformation, following exhumation below the thinned Afghan Block margin (Angiboust et al., 2013; Bonnet et al., 2018).

The age of the Cheshmeh-e Ostad complex is inferred to be Cenomanian to Campanian, since these plutonic rocks intrude the Albian basement and are overlain by Maastrichtian deposits (biostratigraphic ages from Maurizot et al., 1990a). One tonalite from the Cheshmeh-e Ostad complex gave a similar Campanian K-Ar date at 79.6 ± 3.2 Ma (Maurizot et al., 1990a). The contacts between the plutonic samples #30a and 34 and their surrounding rocks are obscured by younger deposits. Samples #31a, 33, 64, 65 and 67 are lava flows interbedded into the Senonian flysch (Fig. 4a; Tirrul et al., 1983). Samples #20 and 62 are dykes intruding the Senonian flysch (Fig. 4b) which are overlain by a Paleocene reef. We infer that these lavas and dykes have a Senonian age.

In summary, stratigraphic and isotopic constraints suggest that our samples have been emplaced from 86 to 71 Ma (i.e., Santonian-Campanian up to the base of Maastrichtian), slightly after the HP-LT metamorphic peak.

Two samples (#35a and b) collected to the W of the HP-LT units are from a dacitic dyke (#35a) and trachy-dacitic sill (#35b) intruding an unmetamorphosed ophiolitic sequence (Fig. 4c) unconformably overlain by Maastrichtian flysch-like deposits. Since the Sistan ophiolitic sequence is known to have an Early Aptian to Albian age (Babazadeh and De Wever, 2004; Ozsvárt et al., 2020; Zarrinkoub et al., 2012a), we infer that these dykes were emplaced between the Cenomanian and Campanian, like the 86 to 71 Ma adakitic granitoids reported further south (near Sulabest; Zarrinkoub et al., 2012b).

Table 1
Review of the previous geochronological and/or petrological studies of the N Sistan magmatic rocks.

Samples	Chemistry	Location			Age (Ma)	2σ	Method	Reference	Number in Figs. 2 and 3
		lat. (N°)	Long. (E°)	Closest locality					
Basalts	alkaline	31°36′20″	60°11′53″		4.23	±0.14	Ar-Ar (whole rock)	Pang et al., 2012	1
Basalts	alkaline	32°27′25″	60°12′43″		10.1	±0.2	Ar-Ar (whole rock)	Pang et al., 2012	1
Basalts	alkaline	32°29′30″	60°19′34″		11.0	±2	Ar-Ar (whole rock)	Pang et al., 2012	1
Lavas	unknown	33°11′37″	59°33′29″	Neginan	24.9	±1.0	K-Ar (whole rock)	Fauvelet and Eftekhar-Nezhad, 1990	2
Andesite	calc-alcaline	32°38′50″	59°29′12″	Fanood	25.5	±0.1	Ar-Ar (whole rock)	Pang et al., 2013	6
Dacite	calc-alcaline	32°39′25″	59°43′16″	Sarbishe	27.5	±0.2	Ar-Ar (whole rock)	Pang et al., 2013	6
Andesite	calc-alcaline	32°33′10″	59°49′06″	Salmabad	27.7	±0.2	Ar-Ar (whole rock)	Pang et al., 2013	6
Dacite	calc-alcaline	32°38′51″	59°29′19″	Fanood	29.6	±0.2	Ar-Ar (whole rock)	Pang et al., 2013	6
Dacite	calc-alcaline	32°57′22″	59°19′49″	Markuh	31.0	±0.5	Ar-Ar (whole rock)	Pang et al., 2013	6
Basalts	calc-alcaline			Mood	31.4		K-Ar (whole rock)	Jung et al., 1983	8
Dacite	calc-alcaline	32°55′16″	59°19′26″		31.4	±0.4	Ar-Ar (whole rock)	Pang et al., 2013	6
Monzonite	calc-alcaline	31°07′06″	59°17′52″		33	±1	Rb-Sr (whole rock)	Arjmandzadeh and Santos, 2014	3
Quartz monzonite	calc-alcaline	31°44′33″	59°00′54″		33.3		Rb-Sr (whole rock)	Karimpour et al.,2011	4
Andesite	calc-alcaline	32°25′26″	59°15′41″	Mansoor Abad	37.1	±0.2	Ar-Ar (whole rock)	Pang et al., 2013	6
Monzogranite	calc-alcaline	32°22′30″	58°58′40″		38.2	±0.8	U-Pb (Zr)	Karimpour et al., 2011	4
Monzogranite	calc-alcaline	32°28′04″	58°53′34″		39		U-Pb (Zr)	Karimpour et al., 2011	4
Andesite	calc-alcaline	32°46′39″	59°02′34″		39.1	±0.7	Ar-Ar (whole rock)	Pang et al., 2013	6
Andesite	calc-alcaline	32°25′26″	59°01′50″	Govalg	39.1	±0.5	Ar-Ar (whole rock)	Pang et al., 2013	6
Andesite	calc-alcaline	32°42′59″	59°13′00″		39.4	±0.4	Ar-Ar (whole rock)	Pang et al., 2013	6
Andesitic rocks	calc-alcaline	32°39′40″	59°40′38″		39.5	±0.6	Ar-Ar (whole rock)	Pang et al., 2013	6
Quartz Diorite	calc-alcaline	32°25′50″	59°03′10″		39.6	±0.9	U-Pb (Zr)	Abdi and Karimpour, 2013	7
Quartz Diorite	calc-alcaline	32°26′50″	59°02′50″		39.7	±0.7	U-Pb (Zr)	Abdi and Karimpour, 2013	7
Monzonite	calc-alcaline	31°44′46″	59°01′06″	Chah-Shaljami	40.5	±2	Rb-Sr (whole rock)	Kluyver et al., 1978	5
Dacite	calc-alcaline	32°57′48″	59°32′02″	Khoshineh	42.6	±0.5	Ar-Ar (whole rock)	Pang et al., 2013	6
Dacite	calc-alcaline	32°21′48″	60°23′07″	Doroh	44.4	±0.6	Ar-Ar (whole rock)	Pang et al., 2013	6
Granodiorite	calc-alcaline	31°51′10″	60°14′35″		58.6	±2.1	U-Pb (Zr)	Delavari et al., 2014	9
Tonalite	unknown	33°11′43″	60°14′26″	Sabz kuh	79	±3.2	K-Ar (whole rock)	Maurizot et al., 1990b	10
Tonalite	unknown	32°17′25″	60°48′35″		79.4	±3.2	K-Ar (whole rock)	Maurizot et al., 1990a	11
Granitoide	adakitic			Chah-e-Mehzrab	86.0–71.5	±0.8–0.6	U/Pb Zircon	Zarrinkoub et al., 2012b	12
Granitoide	adakitic			Ratuk-e-Pa'in	86.0–71.5	±0.8–0.6	U/Pb Zircon	Zarrinkoub et al., 2012b	12
Tonalite	unknown	33°20′4″	60°07′27″	Mo'inabad	83.6	±2.6	K-Ar (whole rock)	Maurizot et al., 1990b	10
Gabbro	tholeitic	32°17′32″	59°51′10″		106.9	±1.1	U/Pb Zircon	Zarrinkoub et al, 2012a	13
Gabbro	tholeitic	32°33′54″	59°04′43″		112.8	±0.9	U/Pb Zircon	Zarrinkoub et al, 2012a	13
Chert in ophiolite		33°31′30″	60°18′30″		112		Radiolarian	Babazadeh and De Wever, 2004	14
Chert in ophiolite		33°31′30″	60°18′30″		102 ± 4		Radiolarian	Babazadeh and De Wever, 2004	14
Chert in ophiolite		33°31′30″	60°18′30″		112 ± 12		Radiolarian	Babazadeh and De Wever, 2004	14

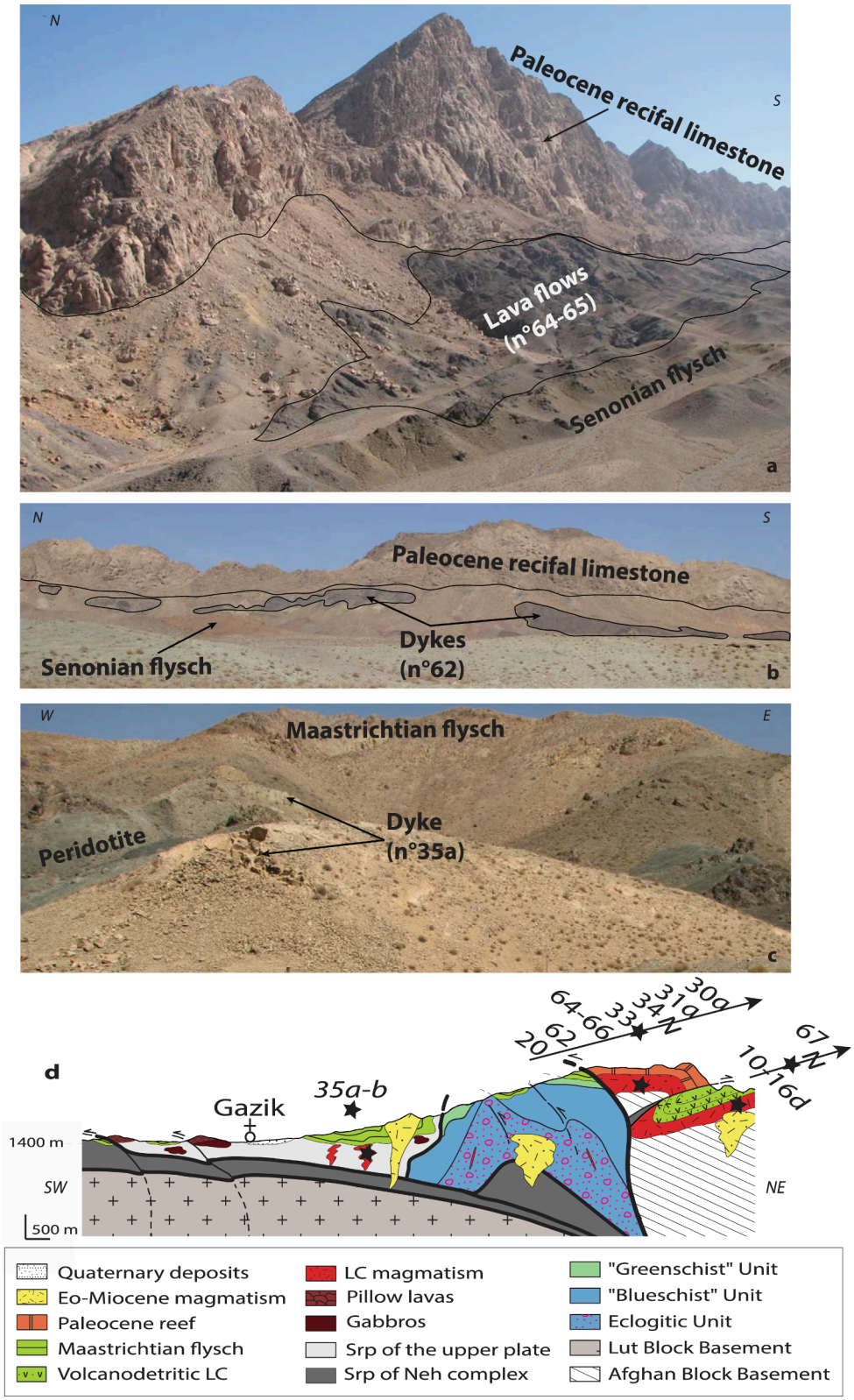

Fig. 4. Structural information. Three landscape photos illustrating the structural position of the Late Cretaceous magmatism. (a) Samples #64 and #65 are lava flows interbedded into the Seonian flysch and below the Paleocene reef. (b) Sample #62 are dyke intrusive into the Senonian flysch and below the Paleocene reef. (c) Dyke #35a intrusive into peridotite and below the Maastrichtian flysch. (d) Synthetic cross-section (located on Fig. 2a) in the Gazik area based on Bonnet et al. (2018) and extended to the W by our field observations. The relative position of our samples (black stars) is reported on it. Above the cross-section, the arrows indicate the relative S to N position of each sample against the Gazik cross-section marked on these arrows by a black star. Srp: serpentinite; LC: Late Cretaceous.

3.2. Petrographic description

Sample locations and petrographic descriptions (mineral occurrences, textural characteristics) are given in Table 2 and Fig. 2. Representative examples are shown in Fig. 5.

— The mafic samples (#10, 11, 14, 16a, 31a, 65) are basaltic lavas flows. They exhibit typical aphanitic texture with plagioclase, Fe-Ti oxide and clinopyroxene microlites. Sample #14 also contains microlitic olivine. Samples #10 and 11 show intersertal texture and sample #65 shows fluidal texture (Fig. 5). Sample #16a is the only porphyric

Table 2
Mineral assemblages and the textural characteristics. Abbreviations from Whitney and Evans (2010).

N°	Differentiation	Position	Sample	Texture	Igneous minerals	Alteration minerals	GPS coordinates	
							Lat. (N°)	Long. (E°)
10	mafic	Lava	Basalt	Intersertal	Pl, Fe-Ti-Ox, Cpx	Ep, Chl, Cal	32°10′09.0″	60°49′33.0″
11	mafic	Lava	Basalt	Intersertal	Pl, Fe-Ti-Ox, CPX	Chl, Act/Tr, Ep	32°10′09.8″	60°50′33.4″
14	mafic	Lava	Basalt	Microphaneritic	Pl, Fe-Ti-Ox, Ol, Cpx	Chl, Ep	32°09′27.7″	60°50′18.0″
16a	mafic	Lava	Basalt	Microphaneritic	Pl, Cpx, Fe-Ti-Ox	Chl	32°09′35.0″	60°50′023.4″
31a	mafic	Lava	Basalt	Microphaneritic	Pl, Qz, Fe-Ti-Ox	Ep	33°20′13.8″	60°06′20.4″
15	intermediate	Dyke	Andesite	Intersertal	Pl, Qz, Fe-Ti-Ox	Chl, Prh, Pump	32°09′27.7″	60°50′18.0″
20	intermediate	Dyke	Basaltic-andesite	Agglomerate	Pl, Fe-Ti-Ox,Ttn	Ep, Cal, Chl, clay	32°18′45.7″	60°34′09.8″
66	intermediate	Dyke	Andesite	Aphanitic porphyric	Pl	Chl, Cal, Prh, Qz, Fe-Ti-Ox	32°40′47.9″	60°23′51.7″
65	intermediate	Lava	Basaltic-trachy-andesite	Fluidal	Pl, Fe-Ti-Ox, Qz	Cal, clay	32°39′52.6″	60°21′29.0″
30a	intermediate	Pluton	Quartzitic-diorite	Phaneritic	Qz, Pl, Amp, Bt, Fe-Ti-Ox		33°20′31.7″	60°07′08.9″
12a	felsic	Dyke	Rhyolite	Aphanitic porphyric	Qz, Pl, K-Fsp, Fe-Ti-Ox	Zeo, Pump, Prh, Chl	32°10′09.8″	60°50′33.4″
12b	felsic	Dyke	Rhyolite	Aphanitic porphyric	Qz, Pl, K-Fsp, Fe-Ti-Ox	Chl, Prh, Pump, Zeo	32°10′09.8″	60°50′33.4″
35a	felsic	Dyke	Dacite	Aphanitic porphyric	Pl, Fe-Ti-Ox		33°00′41.5″	60°13′55.5″
62	felsic	Dyke	Trachy-dacite	Microphaneritic	Pl, Qz, Amp, Fe-Ti-Ox	Chl, Cal, Prh	32°30′39.6″	60°23′26.2″
33	felsic	Lava	Rhyolite	Aphanitic porphyric	Qz, Pl, K-Fsp	Cal, Chl	33°08′11.7″	60°18′09.7″
35b	felsic	Lava	Trachy-dacite	Microphaneritic	Pl, Qz, Fe-Ti-Ox, Amp	clay, Cal, Chl	33°00′41.5″	60°13′55.5″
64	felsic	Lava	Dacite	Microphaneritic porphiric	Pl, Qz, Amp	Chl, Cal	32°39′52.6″	60°21′29.0″
67	felsic	Lava	Rhyolite	Aphanitic porphiric	Pl, Qz, K-Fsp, Fe-Ti-Ox	clay, Cal, Prh	32°42′25.0″	60°29′19.5″
13	felsic	Pluton	Granitoid	Phaneritic	Qz, Pl, K-FSp, Fe-Ti-Ox, Amp	Chl, Prh	32°09′49.2″	60°50′27.8″
16b	felsic	Pluton	Granitoid	Microphaneritic	Qz, K-Fsp, Fe-Ti-Ox, Pl, Ttn	Chl, Pump	32°09′35.0″	60°50′023.4″
16c	felsic	Pluton	Granitoid	Microphaneritic	Qz, Pl, K-Fsp, Fe-Ti-Ox	Prh, Chl	32°09′35.0″	60°50′023.4″
16d	felsic	Pluton	Granitoid	Microphaneritic	Qz, Pl, K-, Fe-Ti-Ox	Ep,Chl	32°09′35.0″	60°50′023.4″
34	felsic	Pluton	Granitoid	Phaneritic	Qz, Pl,K-Fsp, Amp, Bt, Fe-Ti-Ox, Mc	Chl	33°11′56.1″	60°14′06.7″

rock with some phenocrysts of plagioclase and clinopyroxene.

— The intermediate samples, less abundant, are represented by one basaltic-andesite dyke (#20), two andesitic dykes (#15, 66) and one quartz-diorite (#30a). The lava texture varies from typical porphyric for sample 66 to fluidal (#65), intersertal (#15) or aphanitic (#20). Lavas host plagioclase and quartz as microlites. Former Fe-Mg-bearing minerals could not unambiguously be determined as they were transformed into chlorite. Samples #20 and 35b have Fe-Ti oxide and sample #20 comprises titanite. The quartz-diorite (#30a, Fig. 5) has a phaneritic texture with plagioclase, amphibole, biotite and Fe-Ti-oxide phenocrysts.

— The felsic samples are represented by one trachy-dacite (#35b), one dacite (#64) and two rhyolitic (#33 and 67) lava flows, one trachy-dacite (#62), one dacitic (#35a) and two rhyolitic (#12a and 12b) dykes and five granitoids (#13, 16b, 16c, 16d and 34). The two trachy-dacites exhibit microphanitic textures with plagioclase, amphibole, quartz and Fe-Ti oxide phenocrysts. The two dacites are mainly aphanitic but display some plagioclase and amphibole phenocrysts. Sample #64 also exhibits some microlites of quartz and #35a some Fe-Ti oxides. The rhyolites have a porphyric texture with phenocrysts of plagioclase, quartz, alkali-feldspar and Fe-Ti oxide (not present in #33) in a microlitic matrix. All granitoids have a coarse grained granular texture with plagioclase, quartz, alkali feldspar and Fe-Ti oxide associated with titanite in #16b, with amphibole in #13 and 34 and with biotite and muscovite in #34.

All rocks exhibit secondary phases resulting from hydrothermal alteration, more intense in lavas and dykes than in granitoids. Chlorite is present in all samples (Table 2). Prehnite and epidote are also common whereas pumpellyite, zeolite or calcite are only present in a few samples.

4. Analytical methods

Weathered sample rinds were carefully removed to minimize the effect of alteration and a representative fraction of each sample was finely crushed to less than 2 μm grain powder in agate mortars. The protocols used for major, trace elements and isotopic analysis are the same as in Bonnet et al. (2020).

Loss on ignition (LOI) was obtained by routine procedures: around 4 g of powder were heated in an alumina melting-pot at 110 °C during one night at atmospheric pressure, and then weighted. The powder was subsequently heated to 1000 °C for 3 h to release all volatile elements (mostly water), then weighted again. Samples were again weighted after a new heating at 1000 °C for 1 h to ensure all volatile elements had been released. Values given here correspond to less than 1% difference between the last two weights.

The whole-rock major elements analytical procedure is as follows: 50 mg of powder have been digested with 1 ml of concentrated (67%) HNO_3 and 1 ml of HF (47%) in a DigiPREP at 80 °C for 4 h. Then, 48 ml of H_3BO_3 (2%) aqueous solution are quickly added to neutralize excess HF and dissolve the precipitated fluoride. 50 ml of the final clear solutions were obtained and analysed by Inductively Coupled Plasma Optical Emission Spectrometry (ICP-OES at Alipp6 Laboratory, Sorbonne Université, Paris, France, with a Agilent 5100 SVDV ICP-OES). Analytical relative uncertainties are estimated to be better than 5%.

The analytical procedure for trace element begins with the same digestions used in the major elements methodology but the final clear solution obtained was evaporated to dryness. The residual solid was dissolved in 1 ml of H_3BO_3 to neutralize the excess of F, then slowly evaporated to dryness at 60 °C. The residue was dissolved in HNO_3 (2%). The final solutions were diluted by ten and then analysed by Inductively Coupled Plasma Mass Spectrometry (ICP-MS also at Alipp6 Laboratory, Sorbonne Université, Paris, France, with a Agilent 8800 ICP-MS/MS). Analytical relative uncertainties were estimated to be better than 6%.

Calibrations for major and trace elements were made using international standards from the USGS (RGM-1, BIR-1, AGV-2, UB-N, BHVO-2, BCR-1), from MPI-DING (ATho-G) and from SARM-CRPG (BEN-2).

Isotopic ratios $^{143}Nd/^{144}Nd$ and $^{87}Sr/^{86}Sr$ were measured in the SARM-CRPG in Nancy. 150 mg of powder were digested with 4 ml of concentrated (67%) HNO_3 and 1 ml of HF (47%) in a *Savillex* teflon container at 115 °C for 48 h. The solution obtained was evaporated to dryness. The residual solid was dissolved in HCl and digested during 24 h at 125 °C. The clear solution obtained was evaporated to dryness. The

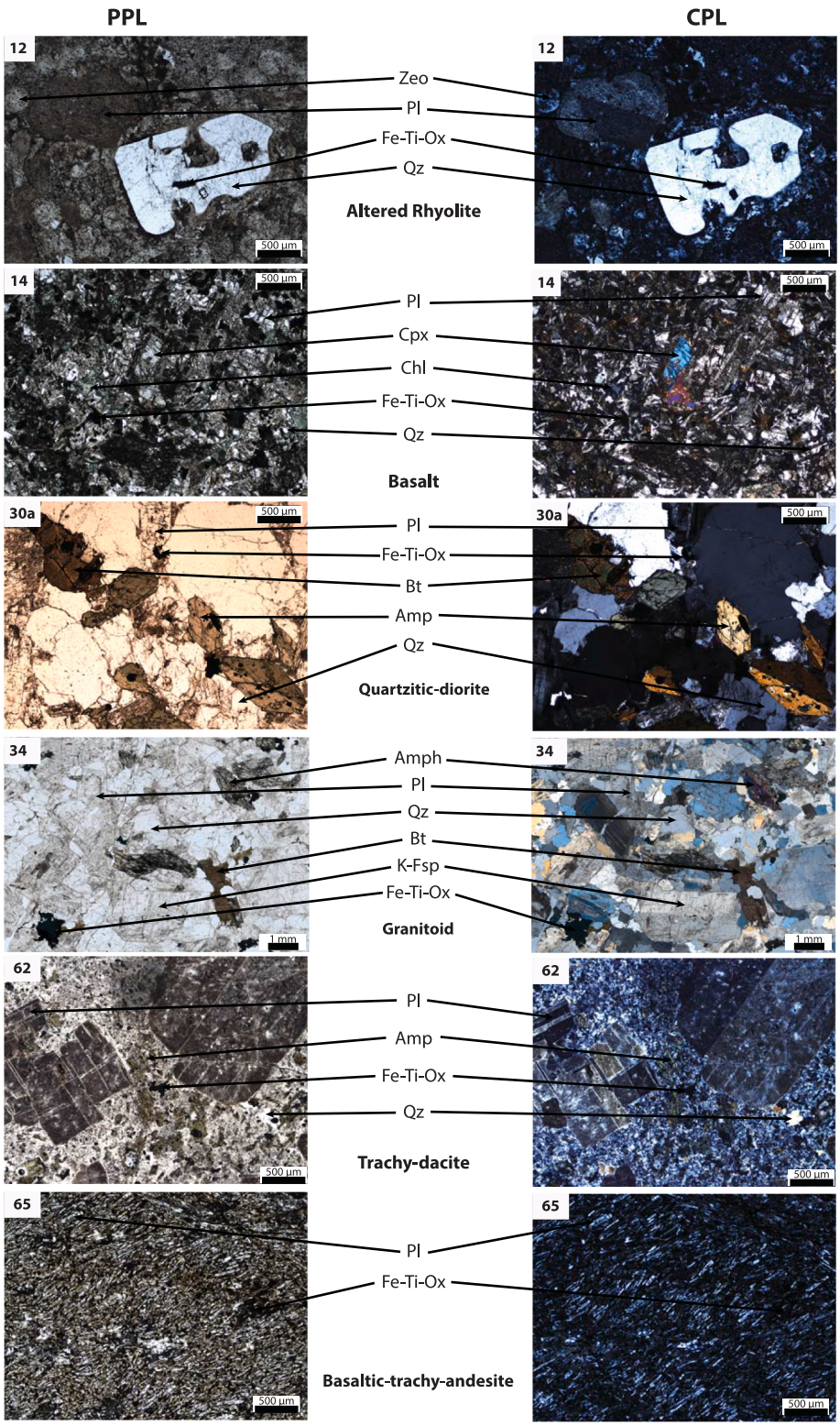

Fig. 5. Thin section photomicrographs in plane polarised light (PPL, on the left) and in crossed polarised light (CPL, on the right) numbers refer to the sample numbering. #12: Rhyolite with microphaneritic texture mainly composed by quartz, plagioclase and Fe-Ti-oxide; accessory phase is zeolite. #14: Basalt with microphaneritic texture mainly composed by plagioclase, clinopyroxene and Fe-Ti-oxide; accessory phases are quartz and chlorite. #30a: Quartzitic-diorite with phaneritic texture mainly composed by plagioclase, biotite, amphibole, Fe-Ti-oxide and quartz. #34 Granitoid with phaneritic texture mainly composed by plagioclase, alkali-feldspar, quartz, amphibole, biotite and Fe-Ti-oxide. #62: Trachy-dacite with microphaneritic texture mainly composed by plagioclase, amphibole, quartz and Fe-Ti-oxide. #65: Basaltic-trachy-andesite with fluidal texture mainly composed by plagioclase and Fe-Ti-oxide; accessory phases are chlorite.

residual solid was dissolved in HNO_3 (2%). Sr, Rb and others REE were separated using both *Sr-Spec* and *Tru-Spec* ion-exchanging resin following the methodology proposed by Pin et al. (1994). Nd and Sm were separated using successively *Sr-Spec*, *Tru-Spec* then *Ln-Spec* ion-exchanging resin following the procedure proposed by Pin and Zalduegui (1997). Sr was loaded on double Re filaments and Sr isotopes were measured by Thermal Ionization Mass Spectrometry (multi-collector Thermo Triton TIMS). Reference material NBS 987 was regularly run and typical blanks are <300 pg. Nd isotopes were measured by Multiple Collector – Inductively Coupled Plasma -Mass Spectrometry (MC-ICPMS Neptune) following the methodology proposed by Luais et al. (1997). Reference material JNdi was regularly run and typical blanks are <100 pg.

εNd and εSr were obtained as following: εNd = 10^4

Table 3
Major and trace elements data (n = 23 samples).

Sample	10	11	12a	12b	13	14	15	16a	16b	16c	16d	20	30a	31a	33	34	35a	35b	62	64	65	66	67
SiO_2	48.79	48.40	72.88	71.63	63.89	50.72	60.87	49.44	69.08	74.56	74.60	53.10	67.07	45.55	70.04	67.14	70.06	63.25	63.94	63.56	53.99	60.72	70.25
TiO_2	0.94	0.75	0.38	0.40	0.83	1.09	1.43	1.25	0.60	0.36	0.35	1.22	0.38	0.64	0.56	0.40	0.25	0.42	0.41	0.75	1.43	0.53	0.61
Al_2O_3	18.62	18.17	14.63	15.03	16.61	18.06	12.49	15.47	13.86	13.75	13.42	15.90	16.38	13.69	14.11	16.06	16.21	16.68	14.89	15.37	18.33	15.98	13.49
FeO_{tot}	9.75	8.17	2.62	2.75	5.16	10.32	10.15	8.39	3.34	2.57	2.38	7.75	3.88	9.42	2.91	3.87	1.25	2.66	3.39	2.93	7.06	3.72	2.88
MnO	0.15	0.19	0.09	0.09	0.10	0.19	0.12	0.16	0.10	0.07	0.09	0.07	0.10	0.20	0.06	0.10	0.04	0.07	0.07	0.06	0.16	0.07	0.05
MgO	6.84	9.00	0.95	1.40	2.00	5.74	6.30	7.72	4.42	0.93	0.90	4.88	2.10	11.03	1.34	2.06	0.72	3.00	2.63	1.77	1.47	3.51	1.03
CaO	9.47	10.52	2.26	2.16	4.99	9.86	2.11	9.67	0.92	2.13	2.53	5.05	5.12	15.93	1.93	4.09	3.56	3.08	2.15	2.31	7.50	5.82	2.75
Na_2O	3.07	2.16	5.52	5.81	3.85	2.82	1.60	2.64	5.02	5.72	5.61	3.83	3.77	1.51	7.15	3.97	3.52	6.25	7.27	5.80	5.45	5.43	6.04
K_2O	0.14	0.00	0.46	0.41	0.45	0.13	0.24	0.21	0.51	0.35	0.34	0.51	1.45	0.04	0.41	1.72	1.68	1.60	0.44	1.28	0.56	0.91	1.08
P_2O_5	0.13	0.09	0.10	0.10	0.28	0.16	0.26	0.17	0.14	0.10	0.10	0.21	0.13	0.14	0.14	0.13	0.13	0.15	0.11	0.18	0.44	0.14	0.13
LOI	3.60	3.00	1.30	1.50	1.90	2.60	5.40	2.90	2.30	1.00	1.10	4.90	0.84	1.80	2.20	1.30	2.80	4.10	2.90	2.40	5.30	5.60	3.10
Sum	101.49	100.46	101.19	101.27	100.07	101.68	100.96	98.02	100.31	101.54	101.42	97.41	101.22	99.95	100.84	100.85	100.21	101.27	98.20	96.40	101.67	102.43	101.40
K_2O/Na_2O	0.04	0.00	0.08	0.07	0.12	0.05	0.15	0.08	0.10	0.06	0.06	0.13	0.38	0.03	0.06	0.43	0.48	0.26	0.06	0.22	0.10	0.17	0.18
$FeO_{tot} + MgO + MnO + TiO_2$	17.68	18.11	4.04	4.64	8.10	17.34	18.00	17.52	8.46	3.93	3.72	13.91	6.46	21.30	4.87	6.43	2.26	6.15	6.49	5.50	10.11	7.83	4.57
XMg	0.41	0.52	0.27	0.34	0.28	0.36	0.38	0.48	0.57	0.27	0.27	0.39	0.35	0.54	0.32	0.35	0.36	0.53	0.44	0.38	0.17	0.49	0.26
Cs	0.23	0.27	0.17	0.15	0.14	0.31	0.17	0.33	0.11	0.11	0.13	0.94	0.48	0.15	0.19	0.43	4.05	1.46	0.26	1.69	0.93	1.02	0.13
Rb	3.89	4.34	4.06	3.67	5.31	3.91	3.81	4.60	3.95	3.04	3.12	15.50	28.53	3.43	4.06	30.39	64.16	56.97	5.60	32.05	26.83	21.46	7.87
Ba	35.1	24.1	28.4	26.5	39.7	72.9	13.0	38.6	27.2	17.5	14.2	14.6	188.4	14.9	15.8	209.6	213.0	132.0	197.3	101.1	75.1	154.5	63.0
Th	1.24	1.29	1.52	1.52	1.23	1.20	1.42	1.33	1.40	1.43	1.50	4.51	4.33	1.33	1.92	3.99	5.30	2.96	1.54	2.84	4.54	1.72	2.22
U	0.32	0.22	0.52	0.44	0.25	0.29	0.60	0.27	0.46	0.42	0.45	1.17	1.23	0.27	0.55	0.99	1.36	0.74	0.53	0.56	1.62	0.52	0.75
Nb	2.57	1.29	2.62	2.76	2.43	2.85	5.45	4.31	10.13	2.39	2.38	5.49	2.88	0.82	5.39	3.13	4.91	2.99	1.84	2.64	5.55	1.89	2.75
Ta	0.11	0.02	0.13	0.13	0.12	0.14	0.34	0.23	0.67	0.14	0.10	0.38	0.18		0.32	0.19	0.32	0.16	0.08	0.16	0.41	0.07	0.14
La	3.15	2.27	7.27	7.01	5.63	4.54	11.75	4.62	13.93	6.63	6.68	14.49	10.71	4.77	8.97	12.93	13.42	8.42	4.50	8.78	19.46	6.21	8.91
Ce	7.77	5.56	17.81	17.52	14.91	11.53	30.79	11.90	36.57	16.57	16.65	35.23	24.05	11.50	20.68	29.08	23.62	17.20	10.24	19.33	49.83	13.42	25.23
Pb	1.29	1.56	3.81	1.43	1.03	3.55	1.50	1.40	1.04	1.62	1.53	8.11	2.66	2.16	2.04	3.13	10.44	5.22	4.62	4.74	6.70	5.58	2.04
Pr	1.01	0.72	2.52	2.52	2.27	1.64	4.68	1.70	5.24	2.36	2.39	4.47	3.06	1.58	2.80	3.79	2.33	1.97	1.20	2.32	6.81	1.66	3.48
Mo	0.11	0.01	0.15	0.21	0.36	0.21	0.87	0.10	0.11	0.43	0.20	0.59	0.30	0.07	0.13	0.40	0.92	0.20	0.12	0.26	1.14	0.26	0.83
Sr	243	186	178	173	230	234	97	195	83	117	107	338	328	267	153	310	368	280	208	538	278	934	71
Nd	5.44	4.27	11.98	12.38	11.82	8.06	23.27	9.24	23.15	11.64	11.50	18.86	12.78	7.93	12.68	15.32	8.37	8.39	5.40	10.18	29.81	7.45	15.63
Sm	1.91	1.77	3.41	3.43	3.68	2.66	7.18	3.19	6.77	3.38	3.45	4.64	2.91	2.18	3.37	3.38	1.61	2.06	1.62	2.56	7.53	2.03	4.11
Zr	51.1	28.1	52.3	61.5	17.5	54.8	79.8	68.6	68.3	51.9	43.5	141.2	11.3	35.8	113.9	10.2	80.6	83.2	28.1	106.0	346.3	48.5	89.5
Hf	1.33	1.05	1.93	2.04	0.76	1.60	2.49	1.99	2.26	2.28	1.82	4.24	0.62	1.21	3.24	0.60	2.24	2.22	0.82	4.03	6.62	1.87	2.83
Eu	0.69	0.52	0.91	0.86	1.08	0.89	2.36	1.09	1.01	0.95	0.99	1.18	0.77	0.68	0.79	0.80	0.46	0.48	0.49	0.79	2.25	0.70	0.77
Gd	2.08	1.87	3.46	3.60	4.24	2.94	8.21	3.52	7.15	3.68	3.49	4.47	2.42	2.08	3.12	2.92	1.23	1.75	1.47	2.46	7.91	1.87	3.89
Tb	0.41	0.40	0.69	0.67	0.74	0.55	1.33	0.66	1.27	0.68	0.62	0.68	0.38	0.35	0.60	0.45	0.21	0.29	0.25	0.40	1.30	0.32	0.64
Dy	2.65	2.70	3.93	3.85	4.89	3.54	8.24	4.37	8.13	4.20	3.97	4.02	2.36	2.09	3.38	2.57	1.08	1.55	1.43	2.32	7.91	1.86	3.90
Li	6.77	4.81	4.83	3.98	6.18	5.93	6.28	5.91	5.25	4.14	3.89	24.89	5.95	4.76	5.86	4.56	23.15	27.41	25.01	8.96	21.94	28.98	9.65
Y	14.97	14.94	21.68	24.61	26.03	19.62	42.62	22.94	42.83	22.72	21.22	21.61	13.74	11.06	18.39	16.03	5.59	7.75	7.04	11.93	41.71	9.30	21.26
Ho	0.60	0.61	0.83	0.90	1.03	0.76	1.64	0.87	1.61	0.87	0.83	0.81	0.49	0.42	0.72	0.58	0.20	0.30	0.29	0.45	1.57	0.38	0.78
Er	1.62	1.65	2.26	2.25	2.69	2.06	4.31	2.42	4.50	2.36	2.34	2.23	1.35	1.11	2.11	1.61	0.54	0.79	0.74	1.22	4.49	1.05	2.28
Tm	0.22	0.24	0.32	0.39	0.39	0.29	0.58	0.32	0.58	0.40	0.34	0.31	0.21	0.19	0.31	0.24	0.08	0.11	0.11	0.17	0.60	0.13	0.31
Yb	1.47	1.43	2.09	2.49	2.24	1.93	3.68	2.16	3.89	2.27	2.93	1.94	1.43	0.95	1.98	1.66	0.51	0.65	0.62	0.95	3.75	0.71	2.00
Lu	0.23	0.22	0.29	0.32	0.31	0.30	0.47	0.30	0.47	0.29	0.30	0.28	0.22	0.15	0.35	0.26	0.08	0.11	0.09	0.14	0.55	0.12	0.31
Sc	41.7	37.0	13.0	14.7	21.3	36.7	17.6	35.2	9.7	14.1	13.1	19.3	11.5	35.8	11.9	11.6	2.8	8.2	10.4	9.4	17.5	14.0	10.2
V	297	209	36	36	49	312	154	230	38.9	26.9	27.1	112.3	88.0	244.5	81.8	84.5	22.0	54.6	62.9	57.0	95.1	90.8	70.7
Cr	13.5	68.5	7.08	2.18	2.82	11.8	3.1	259	15.0	2.33	2.37	48.7	8.91	421	5.28	9.62	13.0	65.9	21.9	13.2	2.22	90.3	6.86
Ga	16.5	15.3	12.9	12.6	17.1	16.7	17.7	16.6	16.1	10.6	8.9	17.7	15.8	14.3	11.7	16.1	14.4	16.4	15.5	15.5	23.6	15.8	13.2
Co	35.11	29.69	3.61	3.47	10.44	32.47	13.46	36.42	3.38	2.87	2.45	25.79	8.55	51.03	5.54	8.51	2.30	11.00	10.20	9.81	16.54	13.96	5.53
Ni	25.7	50.6	2.32	2.05	2.17	18.9	3.77	101	6.96	1.69	2.05	45.1	4.82	286	3.73	4.74	9.88	49.1	12.9	18.6	3.07	31.1	4.25
Cu	91.0	10.2	7.74	14.8	17.9	120	8.64	57.6	6.04	14.6	18.2	36.4	9.66	17.8	24.4	19.1	14.6	18.1	18.3	22.5	61.1	24.3	40.3
Zn	73.1	74.0	55.1	38.9	20.2	100	34.3	66.0	36.2	23.2	34.8	54.9	21.2	109	51.5	27.8	13.3	31.9	35.3	40.6	103	32.4	50.1
Nb/Ta	23.5	58.9	20.8	20.5	20.5	20.4	15.8	18.4	15.1	16.9	23.6	14.3	15.9		16.7	16.7	15.3	18.6	23.2	16.3	13.4	26.5	19.9
Th/Ta	11.4	59.1	12.1	11.3	10.3	8.56	4.11	5.68	2.09	10.1	14.9	11.8	23.9		5.97	21.3	16.5	18.4	19.4	17.5	10.9	24.2	16.1
Sr/Y	16.2	12.5	8.23	7.03	8.85	11.9	2.28	8.50	1.93	5.15	5.02	15.7	23.9	24.2	8.34	19.3	65.8	36.1	29.5	45.1	6.67	100	3.35
La/Sm	1.65	1.28	2.13	2.04	1.53	1.70	1.64	1.45	2.06	1.96	1.94	3.12	3.68	2.18	2.66	3.83	8.34	4.08	2.77	3.43	2.59	3.06	2.17
$(La/Yb)_{N\ PM}$	1.54	1.14	2.49	2.02	1.80	1.68	2.29	1.53	2.57	2.10	1.63	5.36	5.37	3.59	3.25	5.60	19.0	9.26	5.20	6.65	3.72	6.24	3.19
$(La/Lu)_{N\ PM}$	1.43	1.09	2.60	2.29	1.89	1.59	2.58	1.59	3.07	2.36	2.36	5.42	5.17	3.41	2.65	5.21	17.3	8.19	5.18	6.33	3.65	5.42	2.95

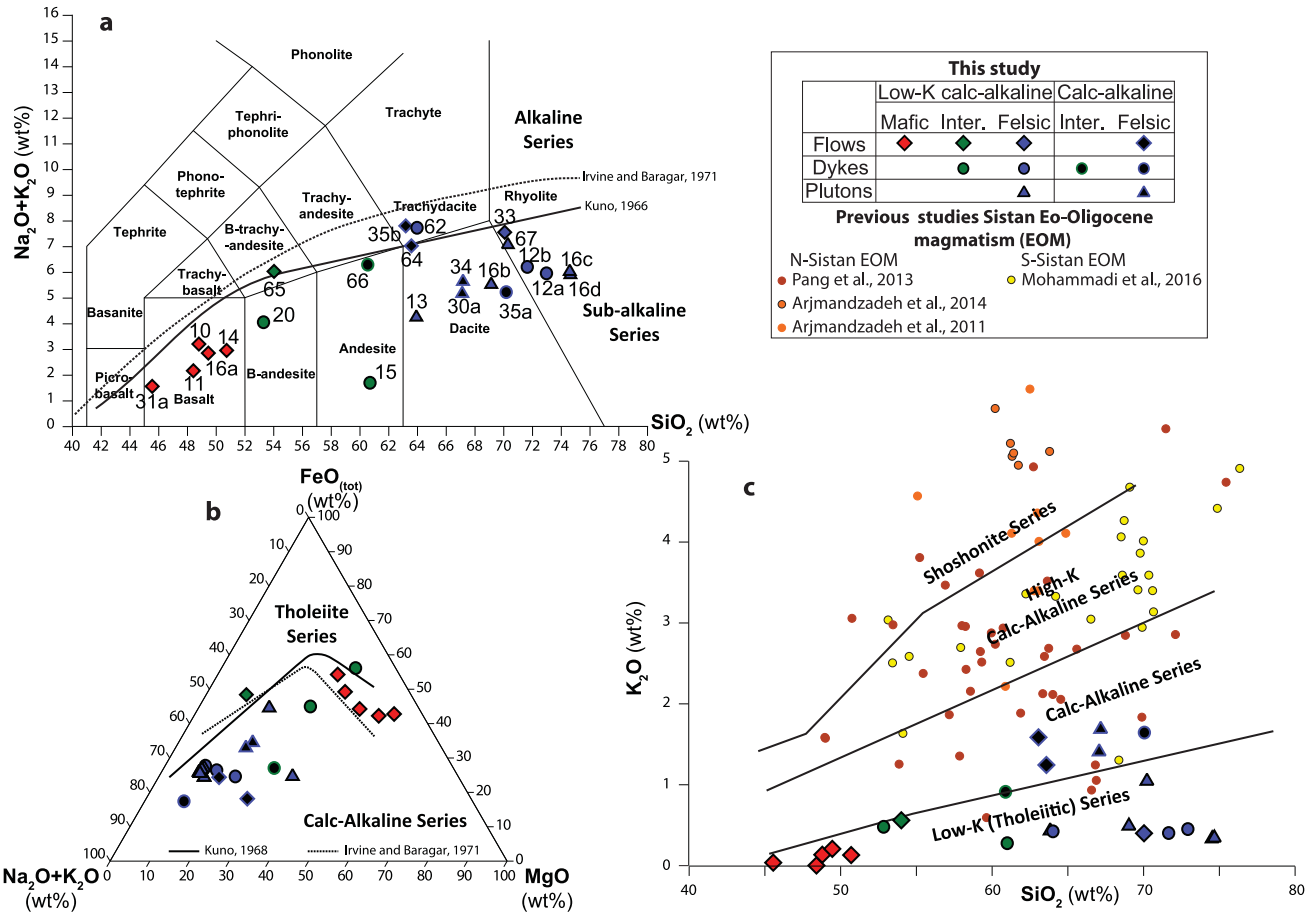

Fig. 6. Chemical classification based on major elements. (a) Total alkali vs SiO_2 (TAS, wt.%) diagram. All the samples plot in the sub-alkaline series field. (b) AFM diagram with our samples on the calc-alkaline trends. (c) K_2O vs SiO_2 (wt.%) diagram showing that our samples are made of two groups: (1) in color, samples on the low-K domain and (2) in black, six samples in the calc-alkaline field. Our data are compared to the Eo-Oligocene calc-alkaline magmatism from the North Sistan (Arjmandzadeh et al., 2011; Pang et al., 2013; Arjmandzadeh and Santos, 2014) and South Sistan (Mohammadi et al., 2016).

$[(^{143}Nd/^{144}Nd)_{(sample)} - (^{143}Nd/^{144}Nd)_{(CHUR)}] / (^{143}Nd/^{144}Nd)_{(CHUR)}$ with value for the actual $(^{143}Nd/^{144}Nd)_{(CHUR)}$ (chondritic uniform reservoir) = 0.512638 (DePaolo and Wasserburg, 1976) and $\varepsilon Sr = 10^4 [(^{87}Sr/^{86}Sr)_{(sample)} - (^{87}Sr/^{86}Sr)_{(CHUR)}] / (^{87}Sr/^{86}Sr)_{(CHUR)}$ with value for the actual $(^{87}Sr/^{86}Sr)_{(CHUR)} = 0.7045$ (Faure and Powell, 1972).

The $^{147}Sm/^{144}Nd_{(t)}$ and $^{87}Rb/^{86}Sr_{(t)}$ values were calculated, using the actual Nd, Sm, Rb and Sr concentrations measured and the isotopic ratio from Roth and Poty (1985) which assume that ^{87}Rb represent 27.83% of the Rb; ^{86}Sr 9.86% of the Sr; ^{147}Sm 15.00% of the Sm and ^{144}Nd 23.83% of the Nd. The concentrations for the present-day CHUR used are: $^{87}Rb/^{86}Sr = 0.0827$, $^{87}Sr/^{86}Sr = 0.7045$, $^{147}Sm/^{144}Nd = 0.1967$, $^{143}Nd/^{144}Nd = 0.512638$. The decay constants used for calculating initial isotopic ratios are after Roth and Poty (1985) with: $\lambda(Rb) = 1.42 \times 10^{-11}$ year^{-1} and $\lambda(Sm) = 6.54 \times 10^{-12}$ year^{-1}. Initial isotopic ratios were calculated as following and assuming a 78 Ma age: $(^{143}Nd/^{144}Nd)_{(78)} = (^{143}Nd/^{144}Nd) \times [(^{147}Sm/^{144}Nd)_{(t)} \times (e^{\lambda(Sm) \times 78} - 1)]$ and $(^{87}Sr/^{86}Sr)_{(78)} = (^{87}Sr/^{86}Sr) \times [(^{87}Rb/^{86}Sr)_{(t)} \times (e^{\lambda(Rb) \times 78} - 1)]$. The same relations were used to calculated $(^{143}Nd/^{144}Nd)_{(BSE\ 78)}$ and $(^{87}Sr/^{86}Sr)_{(BSE\ 78)}$ in order to obtain the $\varepsilon Nd_{(78)}$ and the $\varepsilon Sr_{(78)}$.

5. Major, trace-element and isotopic geochemical data

5.1. Major elements

Major and trace-element compositions of the samples are shown in Table 3. In the total alkali ($Na_2O + K_2O$) vs SiO_2 diagram (TAS diagram; Cox et al., 1979; Fig. 6a), samples plot into the subalkaline field along a fairly linear trend, from basalt to rhyolite. Only sample #15 deviates from the trend, probably because of alteration, as shown by its LOI (5.4 wt%), one of the highest values for our samples. This sample is hereafter only used for trace elements, commonly less affected by alteration (i.e., Tindle and Pearce, 1981; Hastie et al., 2007).

In the AFM diagram (Fig. 6b; Kuno, 1968; Irvine and Baragar, 1971), samples representing liquid compositions together with the plutonic rocks fall on the calc-alkaline trend towards low MgO contents. In the K_2O-SiO_2 diagram (Fig. 6c), most samples (seventeen in total) belong to the low-K calc-alkaline series. Only six samples (shown in black) plot on the medium calc-alkaline domain.

Apart from these six samples, a relatively good inverse correlation is observed for CaO, FeO, Al_2O_3, MgO and MnO vs SiO_2 in Harker diagrams (Fig. 7a-e), or positive correlation for NaO vs SiO_2 (Fig. 7f). Although more scattered, the negative correlation in the CaO/Al_2O_3 vs FeO/MgO diagram (Fig. 7g) suggests fractionation of plagioclase, pyroxene and/or amphibole. The TiO_2 vs SiO_2 plot (Fig. 6h) does not show a correlations probably due to fractionation of Fe-Ti oxides during crystallization of the magma.

5.2. Trace elements

Since trace element analyses do not significant deviate between fresh and the more altered samples, neither in the more mobile LREE nor in mobile elements like Ba and Sr, data for all samples are considered (Table 3). Fig. 8 shows REE normalized to chondrite and multi-element diagrams normalized to the primitive mantle (Sun and McDonough,

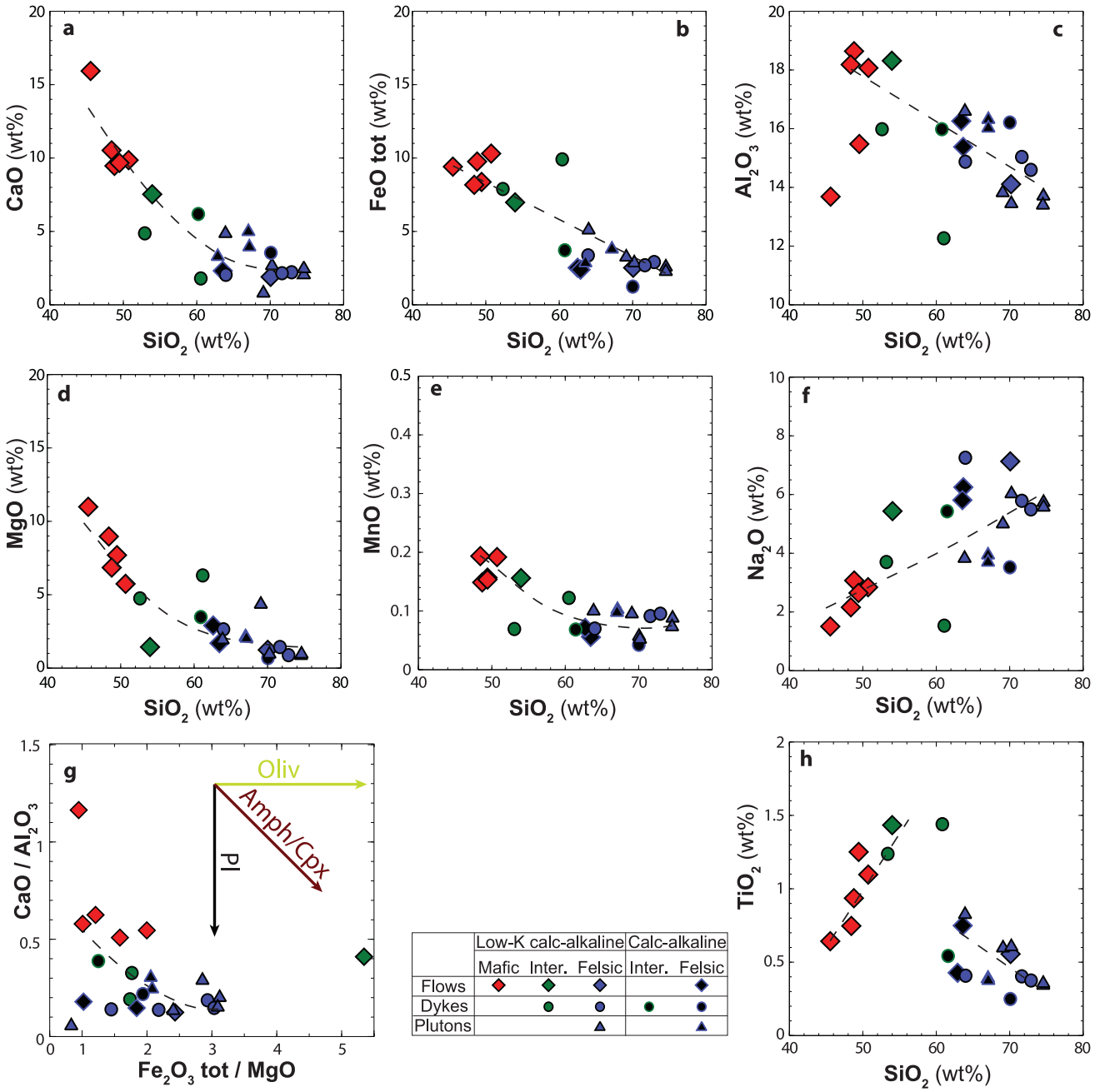

Fig. 7. Binary diagrams showing the variations of selected major elements. (a–f) Respectively CaO, FeO, Al_2O_3, MgO, MnO and Na_2O vs SiO_2 (wt.%) showing in all cases that samples conform with one trend. (g) CaO/Al_2O_3 vs FeO/MgO diagram showing the trends induced by olivine, amphibole and/or plagioclase fractionation. (h) TiO_2 vs SiO_2 (wt.%) showing a dispersion in the data probably due to Ti oxide crystallization.

1989).

5.2.1. Trace element patterns of the low-K series

All samples of the low-K series exhibit relatively flat profiles in HREE and are moderately enriched in LREE (La/Lu_N between 1.1 and 5.6; mean: 2.8; Fig. 8a). These patterns suggest a calc-alkaline nature. All these profiles are parallel in the chondrite normalized REE diagram (Fig. 8a). The most differentiated samples (dacite to rhyolite in TAS diagram, Fig. 6a) have negative Eu anomalies compared to Sm and Gd, in Ba compared to Rb and Th and in Sr compared to Pr and Nd (Fig. 8b), consistent with plagioclase fractionation (Weill and Drake, 1973).

Multi-elementary diagrams exhibit marked negative anomalies in high field strength elements (HFSE) like Nb-Ta-Ti and positive anomalies in large ion lithophile elements (LILE) like Th, U, Pb and K (Fig. 8b) which is classically interpreted by partial melting of a mantle metasomatized by subduction fluids (i.e.: Wilson and Downes, 1991; Aldanmaz et al., 2000; Peccerillo and Lustrino, 2005; Seghedi and Downes, 2011).

The calc-alkaline nature of these rocks is confirmed by the Th/Yb vs Ta/Yb (Fig. 9a), Th/Ta vs Yb/Tb (Joron, 2000; Fig. 9b) and Hf/3-Th-Ta diagrams (Wood et al., 1979; Fig. 9c).

5.2.2. Trace element patterns of intermediate to felsic calc-alkaline samples

The six intermediate to felsic samples (black symbols in Figs. 2b and

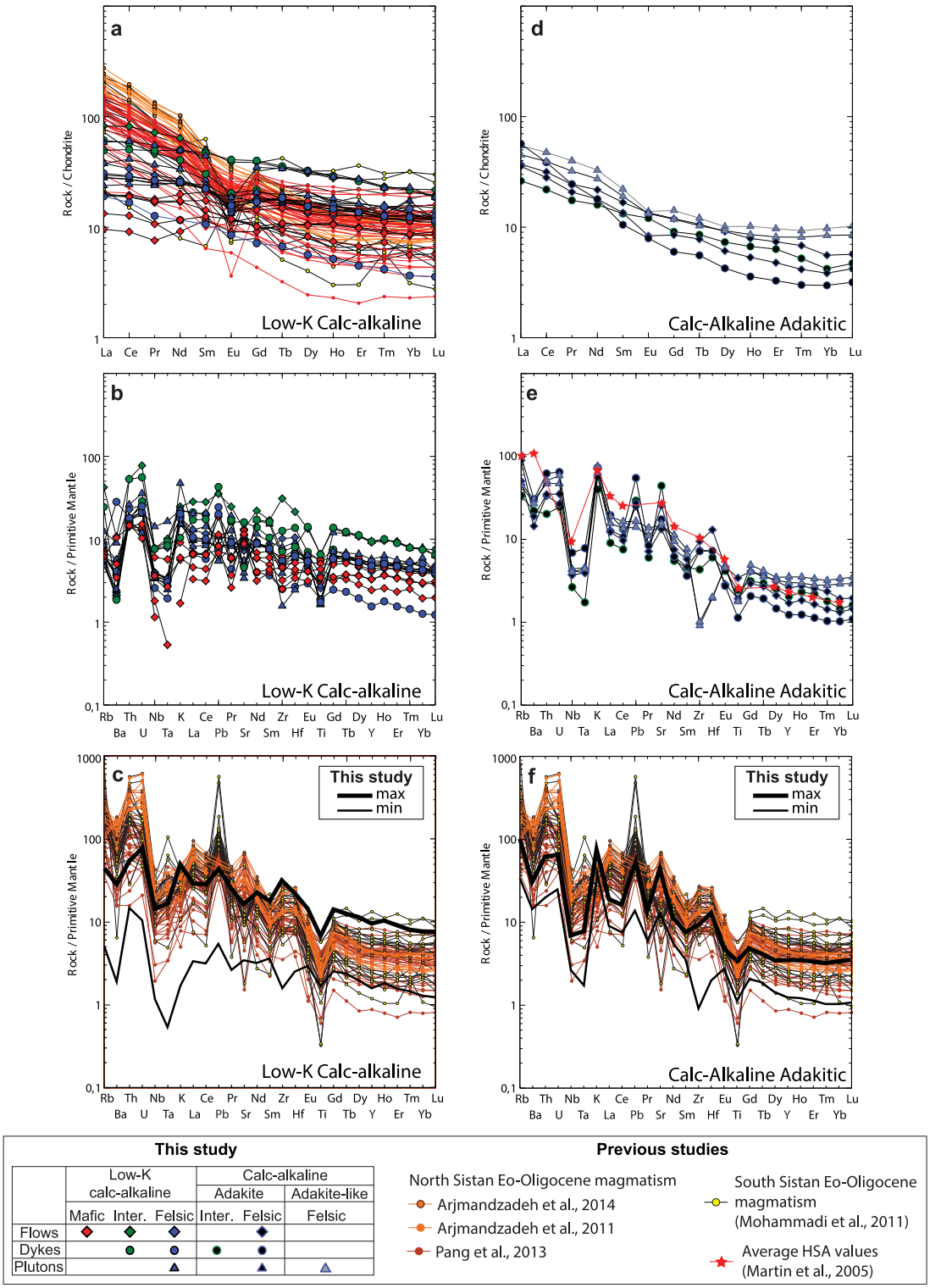

Fig. 8. Multi trace elements diagrams. (a) Rare earth element (REE) patterns normalized to chondritic values (Sun and McDonough, 1989) for the low-K calc-alkaline series compared to Eo-Oligocene of the North and South Sistan (colored thin lines Arjmandzadeh et al., 2011; Pang et al., 2013; Arjmandzadeh and Santos, 2014; Mohammadi et al., 2016). (b) Multi-element diagrams normalized to the composition of the primitive mantle (Sun and McDonough, 1989) for the low-K calc-alkaline series. (c) Multi-element diagrams normalized to the composition of the primitive mantle (Sun and McDonough, 1989) for the low-K calc-alkaline series (between the two black bold lines) compared to Eo-Oligocene of the North and South Sistan (colored thin lines). (d) REE patterns normalized to chondritic values (Sun and McDonough, 1989) for the calc-akaline adakitic rocks compared to the same studies than in a. (e) Multi-element diagrams normalized to the composition of the primitive mantle (Sun and McDonough, 1989) for the calc-akaline adakitic rocks and mean values of high-silica adakite (red stars; Martin et al., 2005). (f) Multi-element diagrams normalized to the composition of the primitive mantle (Sun and McDonough, 1989) for the calc-akaline adakitic (between the two black bold lines) compared to the same studies than in c.

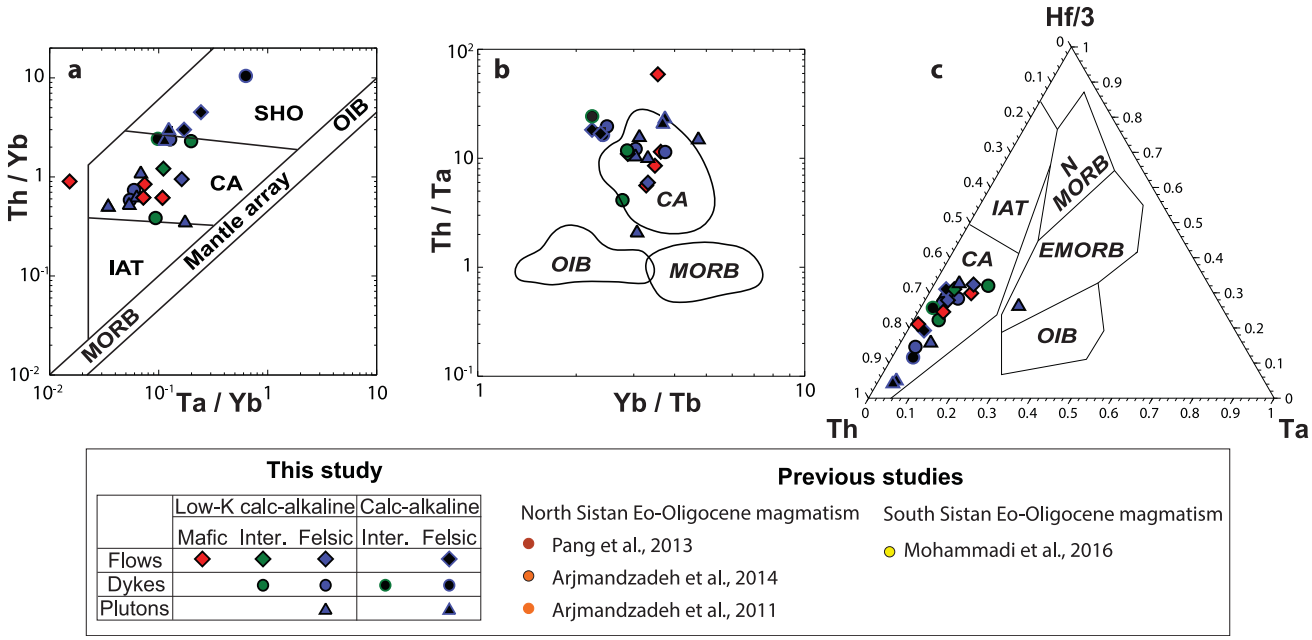

Fig. 9. Chemical classification based on trace elements. (a) Th/Yb vs Ta/Yb (Pearce et al., 1981). (b) Th/Ta vs Yb/Tb (Joron, 2000). (c) Tertiary diagram Th, Ta, Hf/3 (ppm; Wood et al., 1979). CA: Calc-Alkaline; EMORB: Enriched Mid Oceanic Ridge Basalt; IAT: Island Arc Tholeiite; MORB: Mid Oceanic Ridge Basalt; NMORB: Normal Mid Oceanic Ridge Basalt; OIB: Ocean Island Basalts; SHO: Shoshonitite.

6) exhibits very similar chondrite normalized REE patterns, with a strong depletion in HREE and an enrichment in LREE (Fig. 8d; La/Lu_N between 5.3 and 17.3; mean: 8.7). Their multi-elementary diagrams (Fig. 8e) show typical calc-alkaline patterns similar to the former sample group (as also reflected in the plots of Fig. 9). However, their stronger positive anomaly in Sr and K, their low concentration in HREE and higher La/Yb ratios, distinguish them from the low-K calc-alkaline rocks. These samples display higher Th/Yb (Fig. 9a) ratios and are located at the boundary between calc-alkaline and shoshonitic domains.

These samples follow most of the criteria defined by Martin (1999) for true adakites (Table 3): SiO_2 content higher that 56% (dacite in TAS diagram Fig. 6a), Na_2O between 3.5 and 7.5%, Sr higher than 300 ppm, Yb content less than 1.5 ppm, Y less than 18 ppm, Mg/(Mg + Fe) around 0.51, (Fe_2O_3 + MgO + MnO + TiO_2) around 7% and La/Yb ratio relatively high. These samples are also richer in K than the other rocks (Fig. 6b).

The Sr/Y vs Y (Drummond and Defant, 1990; Fig. 10a) and La/Yb vs Yb (Martin, 1986; Fig. 10b) diagrams show that samples #35a, 35b, 64 and 66 plot in the adakitic field. Samples #30a and 34 plot close to but outside the adakitic field. All the other samples lie in the classical calc-alkaline island arc field (Fig. 10a and b).

Considering their major element and incompatible element patterns, we assume that samples #35a, 35b, 64 and 66 are true adakites. Samples #30a and 34 will be grouped together with true adakites since these two samples have most of the characteristics of adakites but will be referred to as adakite-like samples due to their slightly lower Sr/Y ratio. Adakite and adakitic-like samples are in the high-silica adakite domain in the Nb vs SiO_2 and Sr vs (CaO + NaO) diagrams (Fig. 10c and d; Martin et al., 2005).

5.3. Sr and Nd isotopes

The Sr and Nd isotopic compositions of eleven samples are given in Table 4. The measured Sr isotopic ratios range from 0.7039 to 0.7074 and εNd(t) values from 2 to 6.8. On the $\varepsilon Nd_{(i)}$ vs $(^{87}Sr/^{86}Sr)_{(i)}$ diagram (Fig. 11a, calculated for 78 Ma), the low-K calc-alkaline samples are located close to the mixing line between the depleted mantle MORB (DMM) and the global subducting sediments (GLOSS) with less than 5% of GLOSS, whereas the adakites and adakite-like samples have lower values $\varepsilon Nd_{(i)}$ (2.8 and 4 for the adakites) Only one sample (#62) plots at a higher value of $(^{87}Sr/^{86}Sr)_{(i)} = 0.7073$, close to the 0.7075 value estimated for Late Cretaceous seawater (Peterman et al., 1970). This high value can be explained either by strong hydrothermal alteration (Kawahata et al., 2001) or by a higher fraction of GLOSS in the source (more than 1%).

6. Geochemical modelling of incompatible trace elements patterns

6.1. Model parameters

Geochemical modelling is hereafter used to constrain the mantle source(s) of the most primitive basalts (#10–11 and 30a) of low-K calc-alkaline rocks and adakites (#35a, b, 64 and 66). Mantle wedge composition is approximated by a mixture of two components: a "pre-subduction" initial peridotite and a "slab-component," which may corresponds to either fluids or melts released from variably altered oceanic crust and/or sediments (e.g. McDade et al, 2003). The depleted MORB mantle (DMM) from Workman and Hart (2005) is used for the trace element composition of the mantle prior to the initiation of the subduction (i.e., the "pre-subduction" peridotite). Compositions for GLOSS (Plank and Langmuir, 1998) and the N-MORB (Sun and McDonough, 1989) were respectively used for the sedimentary and crustal contributions to the "slab-component".

The composition of oceanic sediment- and crust-derived fluids was estimated by multiplying the mobility of each element determined experimentally by Kogiso et al. (1997), by their concentration. Several proportions of slab fluid versus DMM were tested, with a slab fluid composition made up of 70% N-MORB fluids and 30% GLOSS fluids.

Melts are modelled using either global partition coefficients for GLOSS (Johnson and Plank, 2000) or temperature-dependent coefficients for DMM and N-MORB hydrous melts (Kimura et al., 2009). We estimated hydrous partial modal batch melting at several temperatures ranging from 800 to 1200 °C. Since global partition coefficients depend on source mineralogy, several DMM mineralogies were tested between two end-members: a lherzolitic one with 50% olivine, 23% orthopyroxene, 24% clinopyroxene and 3% aluminous phase (garnet or spinel) and a harzbugitic one with 71% olivine, 23% orthopyroxene, 3% clinopyroxene and 3% aluminous phase (garnet or spinel). Mineralogies

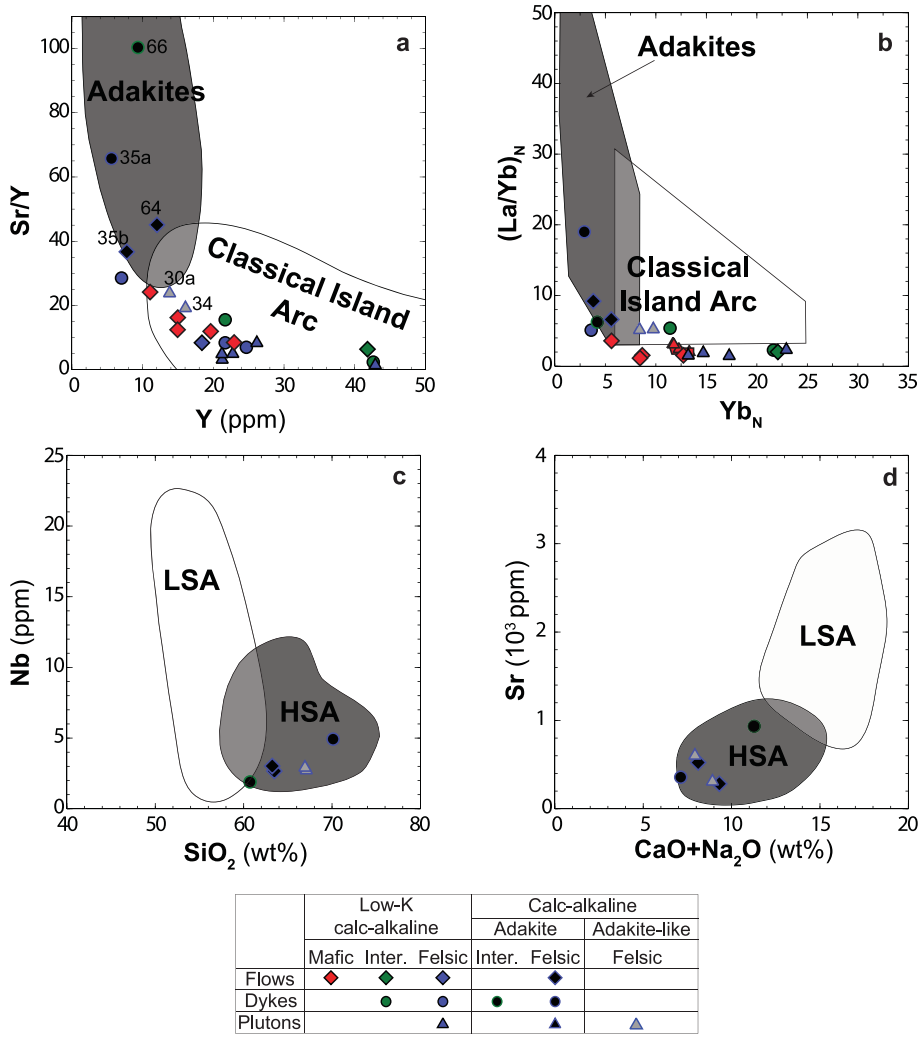

Fig. 10. Binary diagrams used for adakites discrimination. (a and b) Sr/Y vs Y (ppm) (Drummond and Defant, 1990) and $(La/Yb)_N$ vs Yb_N (Martin, 1986); $_N$: normalized to chondrite (Sun and McDonough, 1989) diagrams comparing classical island arc and adakites. (c and d) Nb (ppm) vs SiO_2 (wt%) and Sr (10^3 ppm) vs CaO + NaO (wt.%) diagrams comparing high-SiO_2 adakites (HSA; grey field) and low-SiO_2 adakites (LSA; white field) (Martin et al., 2005).

tested for the oceanic crust range between three end-members: an eclogitic one with 50% garnet and 50% clinopyroxene (E in Fig. 12), an amphibolitic one with 40% amphibole, 40% plagioclase and 20% clinopyroxene (A in Fig. 12) and an eclogite retrogressed in amphibolite with 40% amphibole, 30% garnet and 30% clinopyroxene (AE in Fig. 12).

Modelling was carried out for nineteen elements with well-known partition and mobility coefficients.

6.2. Results

For low-K calc-alkaline primitive basalts (Fig. 12a), the best fits were obtained with 12.5% hydrous partial modal batch melting of a supra-subduction mantle source (SSM-1) at 1 100 °C. The SSM-1 corresponds to a mixture of 90% of DMM source and 10% of slab-derived fluids. Varying the amount of slab-derived fluids from 0 to 20% in the source (grey circles, Fig. 12a) indeed shows that 10% of slab-derived fluids best match the trace element compositions of the primitive basalts. The amount of a sediment component in the magma is thus <5%, in agreement with Sr and Nd isotopic compositions (Fig. 11a).

The mineralogy for the mantle source (SSM-1) giving the best result was obtained for a the garnet-bearing harzburgite end-member. In comparison, the spinel-bearing harzburgite end-member does not reproduce HREE content well, and the garnet-bearing lherzolite end-member underestimates Y content (square and triangle, respectively Fig. 12a). While our best model provides a reasonable fit to the multi-element patterns, subtle differences appear between the lava compositions and those modelled for Rb, Ba, Sr, Th, U and Pb.

Regarding adakites, their PM-normalized trace element patterns are best reproduced by 20% of hydrous partial modal batch melting at 1 100 °C of SSM-2 mantle component made of 95% SSM-1 and 5% of slab melts (Fig. 12b, squares). Varying the amount of slab-derived melts from 0 to 20% in the source induces large variations in the trace element patterns, with a best fit near ~ 5% of slab-derived melts contribution. Slab-melts were assumed to derive from a similar 70%/30% contribution of oceanic crust/sediments. The GLOSS melting is modelled as 5% of a partial melting using the global partition coefficients for each element (Johnson and Plank, 2000). The N-MORB melting is modelled as 3% of a hydrous partial batch melting of an eclogites retrogressed in amphibolite (AE) at 900 °C, consistent with the estimated melt fractions in amphibole-garnet-clinopyroxene rocks at these temperatures (Soret et al., 2017). The amount of amphibole only slightly affects the trace element patterns, but the amphibole is necessary as shown by the model with pure eclogite (triangle, Fig. 12b) which does not satisfactorily reproduce Nd, Sm and Y contents. The mineralogy for the mantle source (SSM-2) giving the best result was again obtained for the garnet-bearing harzburgite end-member. The garnet-bearing lherzolite end-member underestimated Y content (star in Fig. 12b). One model was

Table 4
Sr-Nd isotopic data. The 2σm values are the mean standard deviations of the measurements. A t in index means actual, 78 in index means at 78 Ma (age assumed for this magmatism: initial age).

Sample	$^{143}Nd/^{144}Nd$	2σ (10^{-6})	$^{87}Sr/^{86}Sr$	2σ (10^{-6})	Sm (ppm)	Nd (ppm)	Rb (ppm)	Sr (ppm)	ε Nd (t)	ε Sr (t)	$^{147}Sm/^{144}Nd$ (t)	$^{87}Rb/^{86}Sr$ (t)	$^{143}Nd/^{144}Nd$ (i)	ε Nd (i)	$^{87}Sr/^{86}Sr$ (i)	ε Sr (i)
13	0.512985	8	0.704152	10	3.68	11.82	5.31	230	6.77	−4.94	0.1958	0.0651	0.512885	6.8	0.7041	−4.7
14	0.512971	9	0.704190	8	2.66	8.06	3.91	234	6.50	−4.40	0.2079	0.0471	0.512865	6.4	0.7041	−3.8
16c	0.512974	9	0.704470	8	3.38	11.64	3.04	117	6.55	−0.43	0.1829	0.0734	0.512881	6.7	0.7044	−0.3
30a	0.512907	7	0.703900	10	2.91	12.78	28.53	328	5.25	−8.52	0.1433	0.2455	0.512834	5.8	0.7036	−11.1
31a	0.512960	8	0.704018	8	2.18	7.93	3.43	267	6.28	−6.84	0.1733	0.0363	0.512872	6.5	0.7040	−6.1
33	0.512980	8	0.705110	8	3.37	12.68	4.06	153	6.67	8.66	0.1673	0.0748	0.512895	7.0	0.7050	8.8
34	0.512914	11	0.704093	38	3.38	15.32	30.39	310	5.38	−5.78	0.1388	0.2769	0.512843	6.0	0.7038	−8.9
35a	0.512742	11	0.705213	10	1.61	8.37	64.16	368	2.03	10.12	0.1210	0.4927	0.512680	2.8	0.7047	3.5
62	0.512823	8	0.707407	8	1.62	5.40	5.60	208	3.61	41.26	0.1891	0.0760	0.512727	3.7	0.7073	41.4
64	0.512822	9	0.704934	10	2.56	10.18	32.05	538	3.59	6.16	0.1583	0.1681	0.512741	4.0	0.7047	4.8
65	0.512889	8	0.704812	10	7.53	29.81	26.83	278	4.90	4.43	0.1589	0.2721	0.512808	5.3	0.7045	1.4

performed to represent shallower partial melting using a spinel-bearing SSM-1 mineralogy for the mantle and an amphibolitic mineralogy for the oceanic crust (circle in Fig. 12b). This model overestimates HREE and underestimates Sm and Nd. Despite a reasonably good fit between our best model and adakites compositions, some differences appear for Rb, Ba, Th and U.

7. Discussion: Geochemistry and distribution of the magmatic series

7.1. Low-K calc-alkaline series and constraints on Sistan subduction

7.1.1. Summary of the results

Most samples, as shown by major element diagnostic diagrams (TAS, AFM and K_2O vs SiO_2 Fig. 6), belong to the low-K calc-alkaline type of rocks. Multi-elementary patterns (Fig. 8b) with negative anomalies in HFSE and positive anomalies in LILE confirm their calc-alkaline affinity.

Correlations in Harker diagrams (Fig. 7) suggest that these magmatic rocks are cogenetic: they belong to a single magmatic series derived from the fractional crystallization of a calc-alkaline juvenile magma. The TiO_2 vs SiO_2 and CaO/Al_2O_3 vs FeO/MgO diagrams (Figs. 6h and 7g) suggest that the chemical evolution in this magmatic series is controlled by fractional crystallization of Fe-Ti oxides together with amphibole and/or clinopyroxene in association with plagioclase. The implication of plagioclase during differentiation is also suggested by the negative anomalies in Eu, Ba and Sr (Fig. 8b) in the most differentiated rocks, i.e. the rhyolitic samples (#12a, b, 16c, d, 33 and 67).

In the $\varepsilon Nd_{(i)}$ vs $(^{87}Sr/^{86}Sr)_{(i)}$ diagram (Fig. 11a), the samples from this series lie close to the mixing line between DMM and GLOSS, and their isotopic signature suggests less than 5% of GLOSS. The low-K content and the high $\varepsilon Nd_{(i)}$ value <5 indicate limited contamination by continental crust, as observed mainly in young subduction zones (e.g., Jakes and Gill, 1970; Maury et al., 1996).

These observations are in agreement with the modelling of incompatible trace elements. The best fit is obtained for 12.5% of partial melting of a DMM mixed with 10% of slab-derived fluids (SSM-1, Fig. 12a). No assimilation of continental crust is needed to explain these incompatible patterns. Garnet-bearing harzburgite is needed to reproduce the slope of HREE, suggesting that partial melting took place at >80 km depth for a temperature of 1100 °C. Several factors may explain the differences between the content of Rb, Ba, Sr, Th, U and Pb in the model and in the lavas: (1) source chemistry and/or post melting evolution of the magma (e.g., early plagioclase fractionation) could affect the Rb, Ba and Sr contents; (2) mantle source heterogeneities, whereby variable proportions of accessory minerals may retain these elements (e.g., rutile; Gomez-Tuena et al., 2006); (3) hydrothermal alteration of oceanic crust at/near the oceanic ridge, which particularly affects mobile elements; (4) chemical variability of subducted sediments (e.g., Sr is ~ 4 times higher in E Sunda sediments than in the GLOSS; Plank and Langmuir, 1998).

Our choice of a DMM composition for geochemical modelling is indirectly strengthened by the mostly harzburgitic nature of the Sistan ophiolite mantle (Moazzen et al., 2006; Saccani et al., 2010, Zarrinkoub et al., 2012a). The scarcity of gabbroic bodies and the presence of only thin, discontinuous pillow-lava horizons support a slow-spreading environment for the Sistan ophiolite, suggesting that the mantle source region may correspond to depleted exhumed sub-continental mantle (e.g., Picazo et al., 2016) from the Lut/Afghan blocks.

7.1.2. The low-K calc-alkaline magmatic rocks in their geodynamic context

All the samples from this low-K calc-alkaline magmatic series were collected in the Sefidabeh basin overlying the Afghan block to the E of the suture (Figs. 2 and 4d) and are either intrusive (dykes and plutons) or interbedded (lava flows) into the Senonian flysch (Fig. 4). Since this series forms a volcanic arc emplaced through the Sefidabeh basin, it is concluded that the Afghan Block represents the upper plate of the Sistan

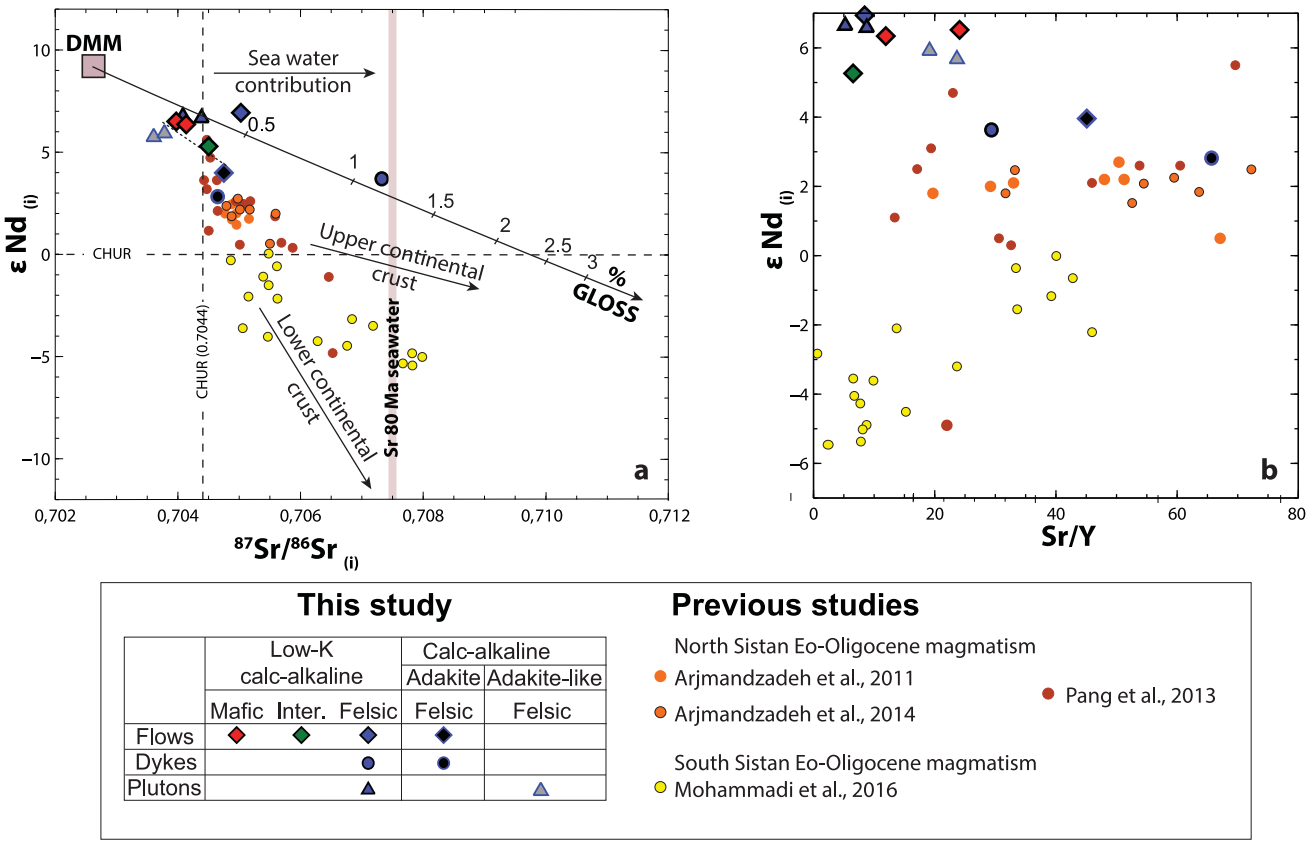

Fig. 11. Binary diagrams showing the Sr-Nd isotopic variations. (a). $\varepsilon Nd_{(i)}$ vs $^{87}Sr/^{86}Sr_{(i)}$. The initial ratio was calculated at 78 Ma for our samples, 40 Ma for those coming from Mohammadi et al. (2016), 33 Ma for those coming from Arjmandzadeh et al. (2011 and 2014), and specific dating ages for those coming from Pang et al. (2013). The field of the subducting sediments is after Plank and Langmuir (1998; GLOSS), the field of the depleted mantle MORB (DMM) is after Workman and Hart (2005), the value for the seawater $^{86}Sr/^{87}Sr$ is after Peterman et al. (1970). (b) $\varepsilon Nd_{(i)}$ vs Sr/Y with the same samples than in a.

subduction zone. This magmatism therefore reflects melting of a mildly metasomatized, highly depleted mantle wedge above a juvenile NE dipping subduction zone. Given the age of the youngest ophiolitic leucogabbro (between 113 ± 1 Ma and 107 Ma; Zarrinkoub et al., 2012a) and of the eclogitic peak (86 ± 3 Ma; Bröcker et al., 2013; Kurzawa et al., 2017; Bonnet et al., 2018), the age of the low-K calc-alkaline magmatism (86–71 Ma) indeed suggests that this magmatic arc formed when the subduction was still relatively young, i.e. <~30 Ma.

7.1.3. Senonian vs Eo-Oligocene magmatism in the Sistan

To further assess subduction polarity (see Section 2.2), Senonian low-K calc-alkaline magmatism has been compared with the calc-alkaline to shoshonitic Eo-Oligocene magmatism (EOM; Fig. 6c) widely distributed across both the Neh complex and the Lut Block (Figs. 1a and 2).

REE patterns of EOM (Fig. 8a-b; thin coloured lines) are relatively flat for HREE but evidence a stronger LREE enrichment compared to our samples. Multi-elementary diagrams show negative anomalies in HFSE and strong positive anomalies in LILE (Fig. 8c, f), but larger amounts of Rb, Ba, Th and U than in our samples. Consistently, the EOM lies in the shoshonitic area in the Pearce diagram (Fig. 9a). In the $\varepsilon Nd_{(i)}$ vs $(^{87}Sr/^{86}Sr)_{(i)}$ diagram (Fig. 11a), the EOM shows higher $(^{87}Sr/^{86}Sr)_{(i)}$ and lower $\varepsilon Nd_{(i)}$ values than our samples. The highest values of $(^{87}Sr/^{86}Sr)_{(i)}$ and lowest values in $\varepsilon Nd_{(i)}$ have been obtained for the South Sistan magmatic rocks (Fig. 11a; Mohammadi et al., 2016; yellow circles).

These characteristics suggest that the EOM results from melting of a strongly metasomatized (phlogopite-bearing) mantle wedge mixed with a crustal component (Arjmandzadeh et al., 2011; Pang et al., 2013; Arjmandzadeh and Santos, 2014; Mohammadi et al., 2016) significantly larger than in the Senonian magmatism reported here. Such an increase in crustal component in EOM would be consistent with crustal thickening following the onset of collision in the Paleocene (in Southern Sistan; Mohammadi et al., 2016) or Eocene (in Northern Sistan; Tirrul et al., 1983), possibly reflecting large-scale lithospheric mantle delamination (Pang et al., 2013; Mohammadi et al., 2016).

7.1.4. Implications for the subduction history

To summarize, our results indicate that, a calc-alkaline magmatic arc was active on the extended margin of the Afghan Block, probably during the Santonian-Campanian in the N Sistan, implying the existence of north-eastward dipping subduction. A schematic reconstruction of the Sistan subduction is prposed in Fig. 13 and further discussed below. In agreement with metamorphic (Fotoohi Rad et al., 2005; Angiboust et al., 2013; Bröcker et al., 2013; Bonnet et al., 2018) and tectonic findings (i.e. Tirrul et al., 1983) we conclude that most if not all of the Sistan ocean was subducted below the Afghan margin. The EOM, largely contaminated by continental crust, would in contrast reflect the collision stage of the orogeny and not a marker of arc magmatism on the Lut block, ruling out the existence of westward dipping subduction. Finally, based on the SSZ nature of some ophiolitic magmas, Saccani et al. (2010) suggested the existence of an additional intra-oceanic subduction during the Late Cretaceous. This suggestion is strengthened by the existence of amphibolite-facies metamorphic soles at the base and to the SW of the Sistan ophiolite, near Hossein Abad.

7.2. Adakitic rocks: Specific insights into subduction dynamics

7.2.1. Summary of the geochemical results on adakites

Adakites (#35a, 35b, 64, 66) and adakite-like (#30a, 34) samples

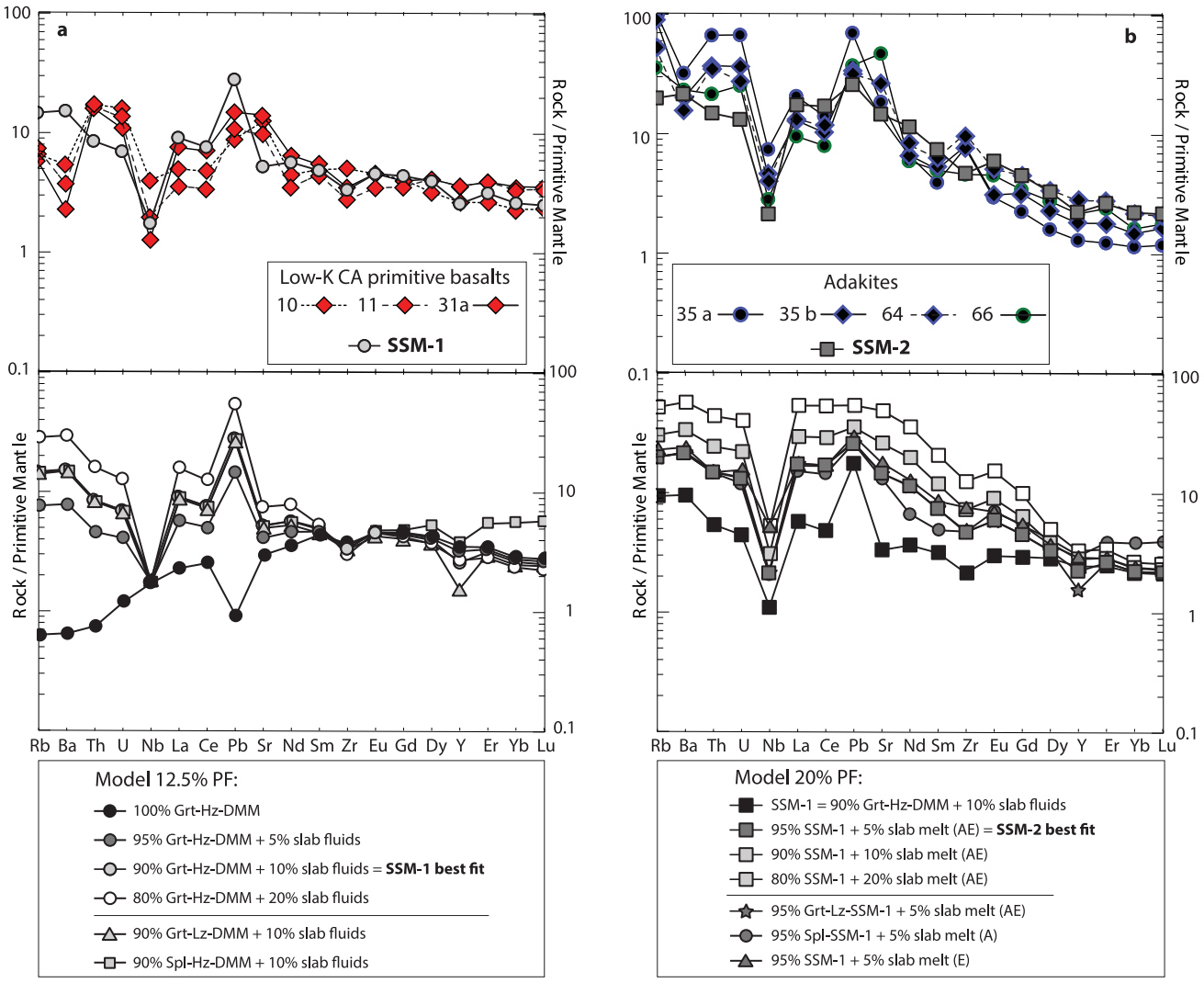

Fig 12. Results of the geochemical modelling. (a) Geochemical modelling of low-K calc-alkaline primitive basalts. On the top: comparison between the most primitive low-K calc-alkaline basalts (selected for their low value in SiO_2 and alkalines) and the best-model obtained by 12.5% of partial melting (PM) of SSM-1 made of 90% DMM metasomatised by 10% of fluids from slab dehydration (see text for more explanation). On the bottom: Comparison of several models highlighting the effect of the amount of slab-derived fluids and of the mantle mineralogy. Percentage of melting, temperature of melting, and chemical composition are always the same. (b) Geochemical modelling of adakites. On top: comparison between the adakites and the best-model obtained by 20% of partial melting (PM) of SSM-2 made of 95% SSZ-1 and 5% melt from slab-derived melts (see text for more explanation). On the bottom: Comparison of several models highlighting the effect of the amount of slab-derived melts and the mantle or oceanic crust mineralogy. Percentage of melting, temperature of melting, and chemical composition are always the same.

exhibit very similar chondrite-normalized REE patterns and are therefore likely cogenetic. These samples are located in the western part of the study area (in places along with low-K calc-alkaline rocks). Isotopic data and geochemical modelling suggest that the low-K calc-alkaline series and the adakites originate from two distinct sources ($\varepsilon Nd_{(i)}$ vs Sr/Y diagram of Figs. 11b and 12).

7.2.2. Origin of adakites

The genesis of adakite has been ascribed to five types of source and/or melting process (Zhang et al., 2019 and references therein). (1) Partial melting of a warm subducted oceanic crust across a narrow P-T window at the garnet amphibolite–eclogite transition, i.e. around 1.5–2.5 GPa and 700–900 °C, with variable contributions from the surrounding metasomatized mantle (e.g., Maury et al., 1996; Martin, 1999; Prouteau et al., 2001; Bourdon et al., 2002; Martin et al., 2005; Hidalgo et al., 2007; Omrani et al., 2008). Adakites produced in this way are high-silica adakites. (2) Partial melting of metasomatized mantle associated with an assimilation of the surrounding rocks, inducing heat consumption and fractional crystallization (AFC process). This generates high-silica adakites too. (3) Partial melting of thickened lower crust in the garnet amphibolite–eclogite facies, associated with significant AFC of mantle-sourced melts, associated with post-collisional delamination (e.g., Stern and Kilian, 1996; Monzier et al., 1999; Xu et al., 2006; Guo et al., 2007). This forms high-Mg adakites belonging to the low-silica adakite group. (4) Partial melting of the thickened lower crust in the garnet amphibolite–eclogite facies without interaction with the mantle, responsible for the formation of high-K adakites. (5) Mixing of a mafic and a felsic magmas in the lower crust. Adakites produced in this way would be high-Mg adakites, low-silica adakites.

Only the first two of these various possibilities produce high-silica adakites as reported here. Option (2) implies the partial melting of a metasomatized mantle associated with significant plagioclase fractionation. However, no characteristic anomaly in Eu is observed in the REE patterns of the studied adakites. The high-silica adakites therefore more likely reflect melting of a metasomatized mantle together with some slab material, generally ascribed to the subduction of a young oceanic

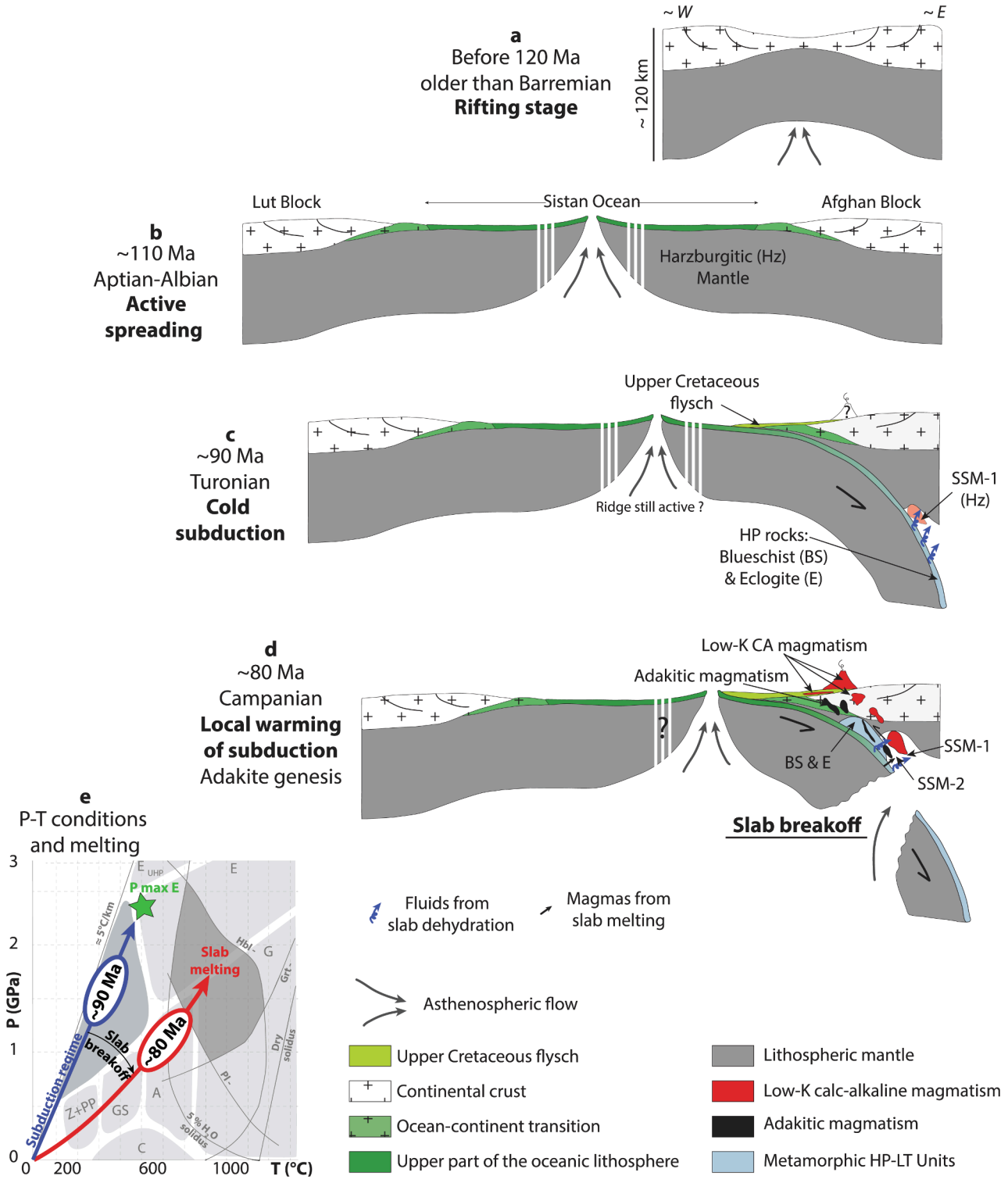

Fig. 13. (a-d) Simplified lithospheric-scale cross-sections showing the evolution through time of the North Sistan. (a) Rifting stage (before 120 Ma, Babazadeh and De Wever, 2004). b) Active spreading stage since the Middle Aptian to Early Aptian (around 110 Ma; Babazadeh and De Wever, 2004; Zarrinkoub et al., 2012a; Ozsvárt et al., 2020). (c) Likely beginning of the subduction stage during the Turonian (around 90 Ma; Angiboust et al., 2013; Bröcker et al., 2013; Kurzawa et al., 2017; Bonnet et al., 2018). (d) Late Cretaceous (~80 Ma) situation with a warming of the subduction zone by slab break-off causing a rise in the asthenosphere upwelling which leads to produce slab melts and high-silica adakite (HSA). e) P-T modified after Martin (1999). The metabasit facies are reported. The diagram displaying the dry and 5% hydrous solidus of tholeiite and some reactions are also drawn: hornblende (Hbl-) garnet (Grt-) and plagioclase (Pl-) out. The grey field is the P-T domain where a magmatic liquid generated by partial melting of a hydrated tholeiite can coexist with a hornblende and garnet-bearing residue without plagioclase: P-T conditions of nowadays HSA generation. The blue line is the metamorphic gradient at 86 Ma estimated at 7.3 °C km^{-1} by Bonnet et al. (2018) and the red line is the geothermal gradients along the Benioff plane need to produce our HSA at ~ 80 Ma. Slab break-off causing a rise in the asthenosphere upwelling which leads to warm the subduction zone, slab melting and high-silica adakite generation is marked by the black arrow.

lithosphere (possibly <~30 Ma; Martin, 1999), as for the Sistan ocean (see 6.1.2), along a warm thermal gradient (i.e.: Peacock et al., 1994; Maury et al., 1996; Martin, 1999; van Keken et al., 2018; Fig. 13e).

This hypothesis is consistent with geochemical modelling results for adakites, since their incompatible trace element patterns are best modelled with a source (SSM-2; Fig. 12b) made of 95% of SSM-1 and 5% of slab melt. In order to reproduce the HREE trend, the SSM-2 mineralogy also requires a garnet-bearing harzburgite for the mantle and an eclogite retrogressed in amphibolite for the oceanic crust, implying partial melting deeper than ~ 80 km. Partial slab melting was modelled at 900 °C, in agreement with the narrow T window proposed by Martin (1999).

7.2.3. Slab-break off or ridge subduction?

The 7.3 °C/km metamorphic gradient estimated for the 86 ± 3 Ma Sistan eclogites (Bröcker et al., 2013; Bonnet et al., 2018) suggests that the subduction thermal regime, prior to adakitic magmatism, was likely too cold to trigger partial melting of the oceanic crust and/or sediments (Fig. 13e, at 90 Ma). Two processes may increase locally the subduction thermal regime: (1) subduction of an oceanic ridge (Defant and Drummond, 1990; Guivel et al., 2006; Tang et al., 2010) or (2) slab break-off and/or slab window (i.e.: Benoit et al., 2002; Guivel et al., 2003; Omrani et al., 2008; Bourgois et al., 2016) allowing for asthenospheric influx and additional heating. Both processes are characterized by a marked, thermally-induced uplift in the upper plate associated with deformation, unconformity and a change in sedimentation towards more proximal deposits (i.e., Bradley et al., 2003; Ramos, 2005; Duretz et al., 2011; Fernández-García et al., 2019). In the Sistan, the Paleocene proximal reef overlying unconformably the Senonian flysch may reflect such a change (Fig. 4a-b). Both processes are also expected to decrease convergence rate and/or promote a change in convergence direction, or favour exhumation of high pressure rocks (Brun and Faccenna, 2008; Agard et al., 2018; van Keken et al., 2018).

Petrological evidence rather supports slab breakoff. First, geochemical modelling shows that the composition of adakites requires melting at 900 °C of a slab component made of both amphibole-bearing retrogressed eclogite and sediment (Fig. 12b), apparently ruling out shallow ridge subduction. Second, some felsic rocks (gneisses) with flat REE patterns were reported amongst the blocks of the eclogite facies subduction mélange (Bröcker et al., 2013; Kurzawa et al., 2017). These gneisses, which are affected by the same amphibolite facies retrograde metamorphism as the eclogites, yielded Rb-Sr isochron ages between ca. 81 and 75 Ma, hence post-dating the eclogite HP-LT peak (i.e., 86 ± 3 Ma). Assuming that these gneisses have a magmatic or mixed metamorphic/magmatic origin (Kurzawa et al., 2017), they could represent felsic melts that have infiltrated the SSM-1 mantle wedge just above the subduction zone. Melting of the mantle (with its additional slab component, SSM-2) requires temperature conditions ≥ 1100 °C, which could be achieved by local mantle upwelling of hot asthenosphere following slab breakoff. This process might also have assisted exhumation of the HP-LT metamorphic rocks and their retrograde metamorphism (Fig. 13d and e).

8. Conclusions

We report the existence of Senonian (86 and 71 Ma) calc-alkaline magmatism emplaced to the E of the Sistan suture zone, mostly within the Afghan Block.

Geochemical data show that two sets of rocks can be distinguished: low-K calc-alkaline rocks and intermediate to felsic high-silica adakitic rocks. Based on their REE and isotopic signature, the low-K calc-alkaline series represents a typical juvenile supra-subduction zone continental arc, with limited interaction with continental crust.

Two distinct sources are needed to reproduce the incompatible trace element patterns through geochemical modelling. The low-K calc-alkaline series requires partial melting of a depleted mantle metasomatized by slab fluids, whereas adakitic compositions require the addition of a fraction (~5 vol%) of melts derived from the amphibole-garnet-bearing oceanic crust and sediments of the Sistan slab.

Formation of this magmatic arc implies NE dipping subduction of the Sistan oceanic lithosphere below the thinned Afghan margin during the Late Cretaceous. The formation of high silica adakites, which slightly postdates the 86 ± 3 Ma peak burial of eclogites along a cold gradient (7 °C km^{-1}), suggests a warming-up of the subduction regime best accounted for by slab breakoff.

CRediT authorship contribution statement

Michael Jentzer: Writing - original draft. **Hubert Whitechurch:** Supervision. **Philippe Agard**: Supervision. **Marc Fournier:** Supervision.

Declaration of Competing Interest

The authors declare that they have no known competing financial interests or personal relationships that could have appeared to influence the work reported in this paper.

Acknowledgements

The authors would like to thank Editor Ibrahim Uysal for the monitoring of the manuscript at different stages. Michael Bröcker, Reza Deevsalar and the third anonymous reviewer are acknowledged for their comments and suggestions, which significantly improved the manuscript. We feel indebted to the Geological Survey of Iran, and especially to Dr. Shahidi, to the geologists and all the staff (drivers, cooks and chief of camp) for their kindness, constant support and for enabling us to visit the region since 2014. This work was financially supported by the CNRS-INSU programs, by ISTeP lab of Sorbonne University and by the overhead of the project "Zooming in Between Plates" (Marie Curie International Training Network of the European Union's Seventh Framework Program FP7/2007/2013/ under REA grant agreement no. 604713). We also would like to warmly thank M. Benoit Villemant who was such a great help to quantify our geochemical analyzes, M. Erwan Martin for taking the time to discuss geochemical results and M. Benoit Dubacq who provided useful corrections to our manuscript.

Appendix A. Supplementary material

Supplementary data to this article can be found online at https://doi.org/10.1016/j.jseaes.2020.104588.

References

Abdi, M., Karimpour, M.H., 2013. Petrochemical characteristics and timing of middle eocene granitic magmatism in Kooh-Shah, Lut Block, Eastern Iran. Acta Geol. Sin. - Engl. Ed. 87, 1032–1044. https://doi.org/10.1111/1755-6724.12108.

Agard, P., Omrani, J., Jolivet, L., Whitechurch, H., Vrielynck, B., Spakman, W., Monié, P., Meyer, B., Wortel, R., 2011. Zagros orogeny: a subduction-dominated process. Geol. Mag. 148, 692–725. https://doi.org/10.1017/S001675681100046X.

Agard, P., Plunder, A., Angiboust, S., Bonnet, G., Ruh, J., 2018. The subduction plate interface: rock record and mechanical coupling (from long to short timescales). Lithos 320–321, 537–566. https://doi.org/10.1016/j.lithos.2018.09.029.

Aldanmaz, E., Pearce, J.A., Thirlwall, M.F., Mitchell, J.G., 2000. Petrogenetic evolution of late Cenozoic, post-collision volcanism in western Anatolia. Turkey. J. Volcanol. Geotherm. Res. 102, 67–95. https://doi.org/10.1016/S0377-0273(00)00182-7.

Angiboust, S., Agard, P., De Hoog, J.C.M., Omrani, J., Plunder, A., 2013. Insights on deep, accretionary subduction processes from the Sistan ophiolitic "mélange" (Eastern Iran). Lithos 156–159, 139–158. https://doi.org/10.1016/j.lithos.2012.11.007.

Arjmandzadeh, R., Karimpour, M.H., Mazaheri, S.A., Santos, J.F., Medina, J.M., Homam, S.M., 2011. Sr-Nd isotope geochemistry and petrogenesis of the Chah-Shaljami granitoids (Lut Block, Eastern Iran). J. Asian Earth Sci. 41, 283–296. https://doi.org/10.1016/j.jseaes.2011.02.014.

Arjmandzadeh, R., Santos, J.F., 2014. Sr-Nd isotope geochemistry and tectonomagmatic setting of the Dehsalm Cu-Mo porphyry mineralizing intrusives from Lut Block, eastern Iran. Int. J. Earth Sci. 103, 123–140. https://doi.org/10.1007/s00531-013-0959-4.

Babazadeh, S.A., De Wever, P., 2004. Early Cretaceous radiolarian assemblages from radiolarites in the Sistan Suture (eastern Iran). Geodiversitas 26, 185–206.
Barrier, E., Vrielynck, B., Bergerat, F., Brunet, M.-F., Mosar, J., Poisson, A., Sosson, M., 2008. Palaeotectonic maps of the Middle East : Tectono-Sedimentary-Palinspastic maps from Late Norian to Pliocene. Darius Programme, Atlas of 14 maps. CCGM.
Barrier, E., Vrielynck, B., Brouillet, J.-F., Brunet, M.-F., 2018. Paleotetconic reconstruction of the Central Tethyan realm. Atlas of 20 maps. CCGM. ISBN: 978-2-917310-30-4.
Benoit, M., Aguillón-Robles, A., Calmus, T., Maury, R.C., Bellon, H., Cotten, J., Bourgois, J., Michaud, F., 2002. Geochemical diversity of late miocene volcanism in Southern Baja California, Mexico: Implication of mantle and crustal sources during the opening of an asthenospheric window. J. Geol. 110, 627–648. https://doi.org/10.1086/342735.
Berberian, F., Berberian, M., 1981. Tectono-plutonic episodes in Iran. Geodyn. Ser. 3, 5–32.
Berberian, M., Jackson, J.A., Qorashi, M., Talebian, M., Khatib, M., Priestley, K., 2000. The 1994 Sefidabeh earthquakes in eastern Iran: blind thrusting and bedding-plane slip on a growing anticline, and active tectonics of the Sistan suture zone. Geophys. J. Int. 142, 283–299.
Besse, J., Torcq, F., Gallet, Y., Ricou, L.E., Krystyn, L., Saidi, A., 1998. Late Permian to Late Triassic palaeomagnetic data from Iran: constraints on the migration of the Iranian block through the Tethyan Ocean and initial destruction of Pangaea. Geophys. J. Int. 135, 77–92. https://doi.org/10.1046/j.1365-246X.1998.00603.x.
Beydokhti, R.M., Karimpour, M.H., Mazaheri, S.A., Santos, J.F., Klötzli, U., 2015. U-Pb zircon geochronology, Sr-Nd geochemistry, petrogenesis and tectonic setting of Mahoor granitoid rocks (Lut Block, Eastern Iran). J. Asian Earth Sci. 111, 192–205. https://doi.org/10.1016/j.jseaes.2015.07.028.
Bonnet, G., Agard, P., Angiboust, S., Monié, P., Jentzer, M., Omrani, J., Whitechurch, H., Fournier, M., 2018. Tectonic slicing and mixing processes along the subduction interface: The Sistan example (Eastern Iran). Lithos 310–311, 269–287. https://doi.org/10.1016/j.lithos.2018.04.016.
Bonnet, G., Agard, P., Whitechurch, H., Fournier, M., Angiboust, S., Caron, B., Omrani, J., 2020. Fossil seamount in southeast Zagros records intraoceanic arc to back-arc transition: New constraints for the evolution of the Neotethys. Gondwana Res. 81, 423–444. https://doi.org/10.1016/j.gr.2019.10.019.
Bourdon, E., Eissen, J.-P., Monzier, M., Robin, C., Martin, H., Cotten, J., Hall, M.L., 2002. Adakite-like Lavas from Antisana Volcano (Ecuador): Evidence for Slab Melt Metasomatism Beneath the Andean Northern Volcanic Zone. J. Petrol. 43 (2), 199–217.
Bourgois, J., Lagabrielle, Y., Martin, H., Dyment, J., Frutos, J., Cisternas, M.E., 2016. A review on forearc ophiolite obduction, adakite-like generation, and slab window development at the chile triple junction area: uniformitarian framework for spreading-ridge subduction. Pure Appl. Geophys. 173, 3217–3246. https://doi.org/10.1007/s00024-016-1317-9.
Bradley, D.C., Kusky, T.M., Haeussler, P.J., Goldfarb, R.J., Miller, M.L., Dumoulin, J.A., Nelson, S.W., Karl, S.M., 2003. Geologic signature of early Tertiary ridge subduction in Alaska, in: Geology of a Transpressional Orogen Developed during Ridge-Trench Interaction along the North Pacific Margin. Special papers Geological Society of America, 19-50. Doi: 10.1130/0-8137-2371-X.19.
Bröcker, M., Fotoohi Rad, G., Burgess, R., Theunissen, S., Paderin, I., Rodionov, N., Salimi, Z., 2013. New age constraints for the geodynamic evolution of the Sistan Suture Zone, eastern Iran. Lithos 170–171, 17–34. https://doi.org/10.1016/j.lithos.2013.02.012.
Brun, J.-P., Faccenna, C., 2008. Exhumation of high-pressure rocks driven by slab rollback. Earth Planet. Sci. Lett. 272, 1–7. https://doi.org/10.1016/j.epsl.2008.02.038.
Camp, V.E., Griffis, R.J., 1982. Character, genesis and tectonic setting of igneous rocks in the Sistan suture zone, eastern Iran. Lithos 15, 221–239.
Cox, K.G., Bell, J.D., Pankhurst, R.J., 1979. The interpretation of igneous rocks. George Allen. ed. Springer. ISBN: 978-0-412-53410-2.
Defant, M.J., Drummond, M.S., 1990. Derivation of some modern arc magmas by melting of young subducted lithosphère. Nature 347 (6294), 662–665.
Delaloye, M., Desmons, J., 1980. Ophiolites and melange terranes in Iran: a geochronological study and its paleotectonic implications. Tectonophysics 68, 83–111.
Delavari, M., Amini, S., Schmitt, A.K., McKeegan, K.D., Mark Harrison, T., 2014. U-Pb geochronology and geochemistry of Bibi-Maryam pluton, eastern Iran: Implication for the late stage of the tectonic evolution of the Sistan Ocean. Lithos 200–201, 197–211. https://doi.org/10.1016/j.lithos.2014.04.015.
DePaolo, D.J., Wasserburg, G.J., 1976. Nd isotopic variations and petrogenetic models. Geophys. Res. Lett. 3, 249–252. https://doi.org/10.1029/GL003i005p00249.
Drummond, M.S., Defant, M.J., 1990. A model for Trondhjemite-Tonalite-Dacite Genesis and crustal growth via slab melting: Archean to modern comparisons. J. Geophys. Res. 95, 21503. https://doi.org/10.1029/JB095iB13p21503.
Duretz, T., Gerya, T.V., May, D.A., 2011. Numerical modelling of spontaneous slab breakoff and subsequent topographic response. Tectonophysics 502, 244–256. https://doi.org/10.1016/j.tecto.2010.05.024.
Faure, G., Powell, J.L., 1972. Strontium Isotope Geology. Springer, New York.
Fauvelet, E., Eftekhar-Nezhad, J., 1990. Explanatory text of the Qayen quadrangle map 1:250,000. GSI.
Fernández-García, C., Guillaume, B., Brun, J.-P., 2019. 3D slab breakoff in laboratory experiments. Tectonophysics 773, 223–228. https://doi.org/10.1016/j.tecto.2019.228223.
Fotoohi Rad, G.R., Droop, G.T.R., Amini, S., Moazzen, M., 2005. Eclogites and blueschists of the Sistan Suture Zone, eastern Iran: A comparison of P-T histories from a subduction mélange. Lithos 84, 1–24. https://doi.org/10.1016/j.lithos.2005.01.007.
Gill, J.B., 2012. Orogenic andesites and plate tectonics., Springer Science & Business Media. ed. Vol 16.
Gomez-Tuena, A., Langmuir, C.H., Goldstein, S.L., Straub, S.M., Ortega-Gutierrez, F., 2006. Geochemical evidence for slab melting in the trans-mexican volcanic belt. J. Petrol. 48, 537–562. https://doi.org/10.1093/petrology/egl071.
Guivel, C., Lagabrielle, Y., Bourgois, J., Martin, H., Arnaud, N., Fourcade, S., Cotten, J., Maury, R.C., 2003. Very shallow melting of oceanic crust during spreading ridge subduction: Origin of near-trench Quaternary volcanism at the Chile Triple Junction: recent Chile triple junction volcanism. J. Geophys. Res. Solid Earth 108. https://doi.org/10.1029/2002JB002119.
Guivel, C., Morata, D., Pelleter, E., Espinoza, F., Maury, R.C., Lagabrielle, Y., Polvé, M., Bellon, H., Cotten, J., Benoit, M., Suárez, M., de la Cruz, R., 2006. Miocene to Late Quaternary Patagonian basalts (46–47°S): Geochronometric and geochemical evidence for slab tearing due to active spreading ridge subduction. J. Volcanol. Geotherm. Res. 149, 346–370. https://doi.org/10.1016/j.jvolgeores.2005.09.002.
Guo, Z., Wilson, M., Liu, J., 2007. Post-collisional adakites in south Tibet: Products of partial melting of subduction-modified lower crust. Lithos 96, 205–224. https://doi.org/10.1016/j.lithos.2006.09.011.
Hastie, A.R., Kerr, A.C., Pearce, J.A., Mitchell, S.F., 2007. Classification of altered volcanic island arc rocks using immobile trace elements: Development of the Th–Co discrimination diagram. J. Petrol. 48, 2341–2357. https://doi.org/10.1093/petrology/egm062.
Hidalgo, S., Monzier, M., Martin, H., Chazot, G., Eissen, J.-P., Cotten, J., 2007. Adakitic magmas in the Ecuadorian Volcanic Front: Petrogenesis of the Iliniza Volcanic Complex (Ecuador). J. Volcanol. Geotherm. Res. 159, 366–392. https://doi.org/10.1016/j.jvolgeores.2006.07.007.
Irvine, T.N., Baragar, W.R.A., 1971. A guide to the chemical classification of the common volcanic rocks. Can. J. Earth Sci. 8, 523–548. https://doi.org/10.1139/e71-055.
Jakes, P., Gill, J., 1970. Rare earth elements and the island arc tholeiitic series. Earth Planet. Sci. Lett. 9, 17–28. https://doi.org/10.1016/0012-821X(70)90018-X.
Jentzer, M., Fournier, M., Agard, P., Omrani, J., Khatib, M.M., Whitechurch, H., 2017. Neogene to Present paleostress field in Eastern Iran (Sistan belt) and implications for regional geodynamics: Paleostress Field in Eastern Iran. Tectonics 36, 321–339. https://doi.org/10.1002/2016TC004275.
Johnson, M.C., Plank, T., 2000. Dehydration and melting experiments constrain the fate of subducted sediments: The fate of subducted sediments. Geochem. Geophys. Geosyst. 1 https://doi.org/10.1029/1999GC000014.
Joron, J.-L., 2000. Eléments hygromagmaphiles : concepts, methodes d'etude. Applications à l'étude de la pétrogenèse des magmas et aux propriétés de leurs sources mantelliques. Mise au point et valorisation d'un outil géochimique : l'analyse par activation neutronique. Thèse de doctorat d'Etat. Université Paris VII.
Jung, D., Keller, J., Khorasani, R., Marcks, C., Baumann, A., Horn, P., 1983. Petrology of the Tertiary magmatic activity the northern Lut area, East of Iran. Minist. Mines Met. GSI, geodynamic project (geotraverse) in Iran 51, 285–336.
Karimpour, M., Stern, C. R., Farmer, L., Saadat, S., Malekezadeh, A.1 2011. Review of age, Rb-Sr geochemistry and petrogenesis of Jurassic to Quaternary igneous rocks in Lut Block, Eastern Iran. Geopersia 1, 19–54.
Kawahata, H., Nohara, M., Ishizuka, H., Hasebe, S., Chiba, H., 2001. Sr isotope geochemistry and hydrothermal alteration of the Oman ophiolite. J. Geophys. Res. Solid Earth 106, 11083–11099. https://doi.org/10.1029/2000JB900456.
Kimura, J.-I., Hacker, B.R., van Keken, P.E., Kawabata, H., Yoshida, T., Stern, R.J., 2009. Arc Basalt Simulator version 2, a simulation for slab dehydration and fluid-fluxed mantle melting for arc basalts: Modeling scheme and application: arc basalt simulator. Geochem. Geophys. Geosyst. 10 https://doi.org/10.1029/2008GC002217.
Kluyver, H.M., Griffis, R.J., Tirrul, R., Chance, P.N., Meixner, H.M., 1978. Explanatory Text of the Lakar Kuh Quadrang. GSI.
Kogiso, T., Tatsumi, Y., Shimoda, G., Barsczus, H.G., 1997. High μ (HIMU) ocean island basalts in southern Polynesia: New evidence for whole mantle scale recycling of subducted oceanic crust. J. Geophys. Res. Solid Earth 102, 8085–8103. https://doi.org/10.1029/96JB03892.
Kuno, H., 1968. Basalts: The Poldervaart treatise on rocks of basaltic composition, in: Differentiation of Basalt Magmas. H.H. Hess and A. Poldervaart. pp. 623–688.
Kurzawa, T., Bröcker, M., Fotoohi Rad, G., Berndt, J., Lisker, F., 2017. Cretaceous high-pressure metamorphism and low pressure overprint in the Sistan Suture Zone, eastern Iran: Additional temperature estimates for eclogites, geological significance of U-Pb zircon ages and Rb-Sr constraints on the timing of exhumation. J. Asian Earth Sci. 147, 332–344. https://doi.org/10.1016/j.jseaes.2017.07.051.
Luais, B., Telouk, P., Albaréde, F., 1997. Precise and accurate neodymium isotopic measurements by plasma-source mass spectrometry. Geochim. Cosmochim. Acta 61, 4847–4854. https://doi.org/10.1016/S0016-7037(97)00293-7.
Martin, H., 1986. Effect of steeper Archean geothermal gradient on geochemistry of subduction-zone magmas. Geology 14 (9), 753–756.
Martin, H., 1999. Adakitic magmas: modern analogues of Archaean granitoids. Lithos 46, 411–429.
Martin, H., Smithies, R.H., Rapp, R., Moyen, J.-F., Champion, D., 2005. An overview of adakite, tonalite–trondhjemite–granodiorite (TTG), and sanukitoid: relationships and some implications for crustal evolution. Lithos 79, 1–24. https://doi.org/10.1016/j.lithos.2004.04.048.
Martin, R.F., Piwinskii, A.J., 1972. Magmatism and tectonic settings. J. Geophys. Res. 77, 4966–4975. https://doi.org/10.1029/JB077i026p04966.
Mattei, M., Cifelli, F., Muttoni, G., Rashid, H., 2015. Post-Cimmerian (Jurassic–Cenozoic) paleogeography and vertical axis tectonic rotations of Central Iran and the Alborz Mountains. J. Asian Earth Sci. 102, 92–101. https://doi.org/10.1016/j.jseaes.2014.09.038.

Maurizot, P., Fauvelet, E., Eftekhar-Nezhad, J., 1990a. Explanatory text of the Gazik quadrangle map 1:250,000. GSI.
Maurizot, P., Fauvelet, E., Eftekhar-Nezhad, J., 1990b. Explanatory text of the Shahrakht quadrangle map 1:250,000. GSI.
Maury, R.C., Sajona, F.G., Pubellier, M., Bellon, H., Defant, M.J., 1996. Fusion de la coûte océanique dans les zones de subduction/collision récentes : l'exemple de Mindanao (Philippines). Bulletin de la Société géologique de France 167 (5), 579–595.
McDade, P., Blundy, J.D., Wood, B.J., 2003. Trace element partitioning between mantle wedge peridotite and hydrous MgO-rich melt. Am. Mineral. 88, 1825–1831. https://doi.org/10.2138/am-2003-11-1225.
Moazzen, M., Modjarrad, M., Zarrinkoub, M.H., 2006. Mineral chemistry, petrogenesis and P-T conditions of formation of harzburgitic peridotites from south of Birjand, Eastern Iran. J. Asian Earth Sci. https://doi.org/10.1016/j.jseaes.2005.07.009 (in press).
Moghadam, H.S., Stern, R.J., 2015. Ophiolites of Iran: Keys to understanding the tectonic evolution of SW Asia: (II) Mesozoic ophiolites. J. Asian Earth Sci. 100, 31–59. https://doi.org/10.1016/j.jseaes.2014.12.016.
Mohammadi, A., Burg, J.-P., Bouilhol, P., Ruh, J., 2016. U-Pb geochronology and geochemistry of Zahedan and Shah Kuh plutons, southeast Iran: Implication for closure of the South Sistan suture zone. Lithos 248–251, 293–308. https://doi.org/10.1016/j.lithos.2016.02.003.
Monzier, M., Robin, C., Samaniego, P., Hall, M.L., Cotten, J., Mothes, P., Arnaud, N., 1999. Sangay volcano, Ecuador: structural development, present activity and petrology. J. Volcanol. Geotherm. Res. 90, 49–79. https://doi.org/10.1016/S0377-0273(99)00021-9.
Omidianfar, S., Monsef, I., Rahgoshay, M., Zheng, J., Cousens, B., 2020. The middle Eocene high-K magmatism in Eastern Iran Magmatic Belt: constraints from U-Pb zircon geochronology and Sr-Nd isotopic ratios. Int. Geol. Rev. 1–18 https://doi.org/10.1080/00206814.2020.1716272.
Omrani, J., Agard, P., Whitechurch, H., Benoit, M., Prouteau, G., Jolivet, L., 2008. Arc-magmatism and subduction history beneath the Zagros Mountains, Iran: A new report of adakites and geodynamic consequences. Lithos 106, 380–398. https://doi.org/10.1016/j.lithos.2008.09.008.
Ozsvárt, P., Bahramnejad, E., Bagheri, S., Sharifi, M., 2020. New Albian (Cretaceous) radiolarian age constraints for the Dumak ophiolitic mélange from the Shuru area. Eastern Iran. Cretac. Res. 104451 https://doi.org/10.1016/j.cretres.2020.104451.
Pang, K.-N., Chung, S.-L., Zarrinkoub, M.H., Mohammadi, S.S., Yang, H.-M., Chu, C.-H., Lee, H.-Y., Lo, C.-H., 2012. Age, geochemical characteristics and petrogenesis of Late Cenozoic intraplate alkali basalts in the Lut-Sistan region, eastern Iran. Chem. Geol. 306–307, 40–53. https://doi.org/10.1016/j.chemgeo.2012.02.020.
Pang, K.-N., Chung, S.-L., Zarrinkoub, M.H., Khatib, M.M., Mohammadi, S.S., Chiu, H.-Y., Chu, C.-H., Lee, H.-Y., Lo, C.-H., 2013. Eocene-Oligocene post-collisional magmatism in the Lut-Sistan region, eastern Iran: Magma genesis and tectonic implications. Lithos 180–181, 234–251. https://doi.org/10.1016/j.lithos.2013.05.009.
Paul, A., Hatzfeld, D., Kaviani, A., Tatar, M., Péquegnat, C., 2010. Seismic imaging of the lithospheric structure of the Zagros mountain belt (Iran). Geol. Soc. Lond. Spec. Publ. 330, 5–18. https://doi.org/10.1144/SP330.2.
Peacock, S.M., Rushmer, T., Thompson, A.B., 1994. Partial melting of subducting oceanic crust. Earth Planet. Sci. Lett. 121, 227–244. https://doi.org/10.1016/0012-821X(94)90042-6.
Pearce, J.A., Alabaster, T., Shelton, A.W., Searle, M.P., 1981. The Oman ophiolite as a cretaceous arc-basin complex: evidence and implications. Philos. Trans. R. Soc. Math. Phys. Eng. Sci. 300, 299–317. https://doi.org/10.1098/rsta.1981.0066.
Peccerillo, A., Lustrino, M., 2005. Compositional variations of Plio-Quaternary magmatism in the circum-Tyrrhenian area: Deep versus shallow mantle processes. Special Paper 388: Plates, Plumes and Paradigms. Geol. Soc. Am. 421–434. https://doi.org/10.1130/0-8137-2388-4.421.
Peterman, Z.E., Hedge, C.E., Tourtelot, H.A., 1970. Isotopic composition of strontium in sea water throughout Phanerozoic time. Geochim. Cosmochim. Acta 34, 105–120. https://doi.org/10.1016/0016-7037(70)90154-7.
Picazo, S., Müntener, O., Manatschal, G., Bauville, A., Karner, G., Johnson, C., 2016. Mapping the nature of mantle domains in Western and Central Europe based on clinopyroxene and spinel chemistry: evidence for mantle modification during an extensional cycle. Lithos (in press).
Pin, C., Briot, D., Bassin, C., Poitrasson, F., 1994. Concomitant separation of strontium and samarium-neodymium for isotopic analysis in silicate samples, based on specific extraction chromatography. Anal. Chim. Acta 298, 209–217. https://doi.org/10.1016/0003-2670(94)00274-6.
Pin, C., Zalduegui, J.S., 1997. Sequential separation of light rare-earth elements, thorium and uranium by miniaturized extraction chromatography: Application to isotopic analyses of silicate rocks. Anal. Chim. Acta 339, 79–89. https://doi.org/10.1016/S0003-2670(96)00499-0.
Plank, T., Langmuir, C.H., 1998. The chemical composition of subducting sediment and its consequences for the crust and mantle. Chem. Geol. 145, 325–394. https://doi.org/10.1016/S0009-2541(97)00150-2.
Prouteau, G., Scaillet, B., Pichavant, M., Maury, R., 2001. Evidence for mantle metasomatism by hydrous silicic melts derived from subducted oceanic crust. Nature 410 (6825), 1997–2200.
Ramos, V.A., 2005. Seismic ridge subduction and topography: Foreland deformation in the Patagonian Andes. Tectonophysics 399, 73–86. https://doi.org/10.1016/j.tecto.2004.12.016.
Roth, E., Poty, B., 1985. Méthodes de datation par les phénomènes nucléaires naturels-applications. Masson. ed. ISBN: 2225806748.
Saccani, E., Delavari, M., Beccaluva, L., Amini, S., 2010. Petrological and geochemical constraints on the origin of the Nehbandan ophiolitic complex (eastern Iran): Implication for the evolution of the Sistan Ocean. Lithos 117, 209–228. https://doi.org/10.1016/j.lithos.2010.02.016.
Seghedi, I., Downes, H., 2011. Geochemistry and tectonic development of Cenozoic magmatism in the Carpathian-Pannonian region. Gondwana Res. 20, 655–672. https://doi.org/10.1016/j.gr.2011.06.009.
Soret, Mathieu, Agard, Philipe, Dubacq, Benoît, Plunder, Alexis, Yamato, Philippe, 2017. Petrological evidence for stepwise accretion of metamorphic soles during subduction infancy (Semail ophiolite, Oman and UAE). J. Metamorphic Geol. (in press).
Stern, C.R., Kilian, R., 1996. Role of the subducted slab, mantle wedge and continental crust in the generation of adakites from the Andean Austral Volcanic Zone. Contrib. Mineral. Petrol. 123, 263–281. https://doi.org/10.1007/s004100050155.
Stöcklin, J., 1968. Structural history and tectonics of Iran : a review. Am. Assoc. Pet. Geol. Bull. 52, 1229–1258.
Sun, S., McDonough, W.F., 1989. Chemical and isotopic systematics of oceanic basalts: implications for mantle composition and processes. Geol. Soc. Special Publication 313–345.
Tang, G., Wang, Q., Wyman, D.A., Li, Z.-X., Zhao, Z.-H., Jia, X.-H., Jiang, Z.-Q., 2010. Ridge subduction and crustal growth in the Central Asian Orogenic Belt: Evidence from Late Carboniferous adakites and high-Mg diorites in the western Junggar region, northern Xinjiang (west China). Chem. Geol. 277, 281–300. https://doi.org/10.1016/j.chemgeo.2010.08.012.
Tindle, A.G., Pearce, J.A., 1981. Petrogenetic modelling of in situ fractional crystallization in the zoned Loch Doon pluton. Scotland. Contrib. Mineral. Petrol. 78, 196–207. https://doi.org/10.1007/BF00373781.
Tirrul, R., Bell, I.R., Griffis, R.J., Camp, V.E., 1983. The Sistan suture zone of eastern Iran. Geol. Soc. Am. Bull. 94, 134–150.
van Keken, P.E., Wada, I., Abers, G.A., Hacker, B.R., Wang, K., 2018. Mafic high-pressure rocks are preferentially exhumed from warm subduction settings. Geochem. Geophys. Geosyst. 19, 2934–2961. https://doi.org/10.1029/2018GC007624.
Verdel, C., Wernicke, B.P., Hassanzadeh, J., Guest, B., 2011. A Paleogene extensional arc flare-up in Iran: iranian volcanism. Tectonics 30. https://doi.org/10.1029/2010TC002809.
Walker, R.T., Khatib, M.M., 2006. Active faulting in the Birjand region of NE Iran: active faulting at Birjand in NE Iran. Tectonics 25. https://doi.org/10.1029/2005TC001871.
Walker, R.T., Gans, P., Allen, M.B., Jackson, J., Khatib, M., Marsh, N., Zarrinkoub, M., 2009. Late Cenozoic volcanism and rates of active faulting in eastern Iran. Geophys. J. Int. 177, 783–805. https://doi.org/10.1111/j.1365-246X.2008.04024.x.
Weill, D.F., Drake, M.J., 1973. Europium anomaly in plagioclase feldspar: experimental results and semiquantitative model. Science 180, 1059–1060. https://doi.org/10.1126/science.180.4090.1059.
Whitney, D.L., Evans, B.W., 2010. Abbreviations for names of rock-forming minerals. Am. Mineral. 95, 185–187. https://doi.org/10.2138/am.2010.3371.
Wilson, M., Downes, H., 1991. Tertiary-quaternary extension-related alkaline magmatism in western and central Europe. J. Petrol. 32, 811–849. https://doi.org/10.1093/petrology/32.4.811.
Wood, D.A., Joron, J.-L., Treuil, M., 1979. A re-appraisal of the use of trace elements to classify and discriminate between magma series erupted in different tectonic settings. Earth Planet. Sci. Lett. 45, 326–336. https://doi.org/10.1016/0012-821X(79)90133-X.
Workman, R.K., Hart, S.R., 2005. Major and trace element composition of the depleted MORB mantle (DMM). Earth Planet. Sci. Lett. 231, 53–72. https://doi.org/10.1016/j.epsl.2004.12.005.
Xu, W.-L., Wang, Q.-H., Wang, D.-Y., Guo, J.-H., Pei, F.-P., 2006. Mesozoic adakitic rocks from the Xuzhou-Suzhou area, eastern China: Evidence for partial melting of delaminated lower continental crust. J. Asian Earth Sci. 27, 454–464. https://doi.org/10.1016/j.jseaes.2005.03.010.
Yousefi, E., Friedberg, J.L., 1977. Aeromagnetic Map of Iran. Quaderangle No. F5. GSI.
Zarrinkoub, M.H., Chung, S.L., Chiu, H.Y., Mohammadi, S., Khatib, M., Lin, I.J., 2010. Zircon U-Pb age and geochemical constraints from the northern Sistan suture zone on the Neotethyan magmatic and tectonic evolution in eastern Iran. Abstr. GSA Conf. "Tectonic Crossroads Evol. Orogens Eurasia–Africa–Arabia 520.
Zarrinkoub, M.H., Pang, K.-N., Chung, S.-L., Khatib, M.M., Mohammadi, S.S., Chiu, H.-Y., Lee, H.-Y., 2012a. Zircon U-Pb age and geochemical constraints on the origin of the Birjand ophiolite, Sistan suture zone, eastern Iran. Lithos 154, 392–405. https://doi.org/10.1016/j.lithos.2012.08.007.
Zarrinkoub, M.H., Mohammadi, S.S., Khatib, M.H., 2012b. Evaluation of adakites in the northern part of Sistan suture zone, eastern Iran, for porphyry mineralization. Recent Res. Environ. Geol. Sci. 4.
Zhang, L., Li, S., Zhao, Q., 2019. A review of research on adakites. Int. Geol. Rev. 1–18 https://doi.org/10.1080/00206814.2019.1702592.